

THE LUMINOSITY–SIZE AND MASS–SIZE RELATIONS OF GALAXIES OUT TO $z \sim 3$ ¹

IGNACIO TRUJILLO², GREGORY RUDNICK³, HANS–WALTER RIX², IVO LABBÉ⁴,
 MARIJN FRANX⁴, EMANUELE DADDI⁵, PIETER G. VAN DOKKUM⁶, NATASCHA
 M. FÖRSTER SCHREIBER⁴, KONRAD KUIJKEN⁴, ALAN MOORWOOD⁵, HUUB
 RÖTTGERING⁴, ARJEN VAN DE WEL⁴, PAUL VAN DER WERF⁴, LOTTIE VAN
 STARKENBURG⁴

ABSTRACT

The luminosity–size and stellar mass–size distributions of galaxies out to $z \sim 3$ is presented. We use very deep near–infrared images of the Hubble Deep Field South in the J_s , H , and K_s bands, taken as part FIRES at the VLT, to follow the evolution of the optical rest–frame sizes of galaxies. For a total of 168 galaxies with $K_{s,AB} \leq 23.5$, we find that the rest–frame V–band sizes $r_{e,V}$ of luminous galaxies ($\langle L_V \rangle \sim 2 \times 10^{10} h^{-2} L_\odot$) at $2 < z < 3$ are 3 times smaller than for equally luminous galaxies today. In contrast, the mass–size relation has evolved relatively little: the size at mass $\langle M_\star \rangle \sim 2 \times 10^{10} h^{-2} M_\odot$, has changed by $20(\pm 20)\%$ since $z \sim 2.5$. Both results can be reconciled by the fact that the stellar M/L ratio is lower in the luminous high z galaxies than in nearby ones because they have young stellar populations. The lower incidence of large galaxies at $z \sim 3$ seems to reflect the rarity of galaxies with high stellar mass.

Subject headings: galaxies: fundamental parameters, galaxies: evolution, galaxies: high redshift, galaxies: structure

¹Based on observations collected at the European Southern Observatory, Paranal, Chile (ESO LP 164.O–0612). Also, based on observations with the NASA/ESA *Hubble Space Telescope*, obtained at the Space Telescope Science Institute, which is operated by AURA Inc, under NASA contract NAS 5–26555.

²Max-Planck-Institut für Astronomie, Königstuhl 17, 69117 Heidelberg, Germany

³Max-Planck-Institut für Astrophysik, Postfach 1317, D-85748, Garching, Germany

⁴Leiden Observatory, P.O. Box 9513, NL–2300 RA, Leiden, The Netherlands

⁵European Southern Observatory, D–85748, Garching, Germany

⁶Department of Astronomy, Yale University, P.O. Box 208101, New Haven, CT 06520-8101, USA

1. INTRODUCTION

The size evolution of galaxies with redshift serves as an important constraint on models of galaxy evolution. In the current standard cosmology ($\Omega_M=0.3$, $\Omega_\Lambda=0.7$), hierarchical models of galaxy formation predict a strong increase in the characteristic size of galaxies since $z\sim 3$ (Baugh et al. 1998; Mao, Mo & White 1998; Avila-Reese & Firmani 2001; Somerville, Primack & Faber 2001). This, however, has not yet been extensively tested by observations. Early studies using ground-based telescopes (Smail et al. 1995) and the Hubble Space Telescope (HST; Casertano et al. 1995) showed that at magnitudes of $I \approx 22$ and $R \approx 26$, where the expected median redshift is greater than 0.5, the dominant field population is formed by very small systems with a mean scale length of $\sim 0''.2 - 0''.3$. These objects are more compact than one would expect by assuming a fixed intrinsic physical size (Smail et al. 1995). Subsequent studies (Roche et al. 1998) at fainter magnitudes ($22 < I < 26$) suggested that most size evolution occurs at $z > 1.5$.

The study of galaxy properties at larger redshifts ($z > 2$) was dramatically improved by the identification of a large population of star-forming galaxies (Steidel et al. 1996). These Lyman-Break galaxies (LBGs) are identified by the redshifted break in the far UV continuum caused by intervening and intrinsic neutral hydrogen absorption. Sizes of galaxies at $z \sim 3$ have been measured for LBGs (Giavalisco, Steidel & Macchetto 1996; Lowenthal et al. 1997; Ferguson et al. 2003), but in the rest-frame UV part of their spectra. In the UV these galaxies appear compact ($r \sim 0''.2 - 0''.3$, $\sim 1.5-3 \text{ h}^{-1} \text{ kpc}$), in good qualitative agreement with the predictions for the build-up of stellar mass from hierarchical formation scenarios (Mo, Mao & White 1999). However, the selection technique and the observed rest-frame wavelength raises the following question: are the galaxies selected (Lyman-break galaxies) and the sizes measured (UV sizes) representative of the radial stellar mass distribution of the luminous high- z galaxy population? Put differently, is the radial extent of the instantaneous, relatively unobscured star formation, which is measured by the rest-frame far UV light, indicative of the radial extent of the stellar mass distribution?

To properly test the model predictions one would ideally like to trace the size evolution of galaxies in the optical (rather than UV) rest-frame at every redshift. Any observed size evolution would then reflect true evolutionary changes not subject to the changing appearance of galaxies in different bandpasses, an effect known as the morphological k -correction. Most of the past studies using constant rest-frame bands have been limited to modest redshifts ($z \lesssim 1$; e.g. Lilly et al. 1998) due to the dearth of very deep near infrared images which allow one to reach the rest-frame optical.

To map the size evolution of the stellar body of galaxies it is necessary to conduct an analysis at wavelengths at least as red as the rest-frame optical. At $z \gtrsim 0.8$ this implies

selecting and analyzing galaxies from very deep near-infrared images. In this paper we use data for the Hubble Deep Field South from the Faint InfraRed Extragalactic Survey (FIRES; Franx et al. 2000) to address this issue⁷. We use these data to constrain the size evolution, i.e. we test whether for a given rest-frame luminosity, or a given stellar mass, the sizes of the high- z population are equal to or different from those of nearby galaxies? To assess the degree of evolution, if any, it is crucially important that good local calibrating data be available. With the advent of large local surveys (e.g. the Sloan Digital Sky Survey (SDSS); York et al. 2000), we now have complete samples of local galaxies with accurate measurements of fundamental properties such as luminosity or size to use as low redshift reference points.

This paper is organized as follows: the data and the measurement technique are described in §2; in §3 we present the luminosity-size and mass-size relation of the high- z galaxies and discuss how selection effects play a role in interpreting the observed trends; §4 describes simulations of how the local galaxy population (as provided by the SDSS data) would appear at high- z . By comparing with the FIRES data, we constrain the size evolution for the galaxies in our sample. Finally, in Sect. 5 we discuss our results.

2. OBSERVATIONS, DATA, AND SIZE DETERMINATIONS

2.1. Data and catalog construction

Ultradeep near-infrared images of the Hubble Deep Field South were obtained as part of the FIRES survey and the data processing and photometry are discussed in detail by Labbé et al. (2003)⁸. Briefly, using ISAAC (Moorwood 1997; field of view of $2.5' \times 2.5'$ and pixel scale $0''.119$)⁹ on the VLT the HDF-S was imaged for 33.6 hours in J_s , 32.3 hours in H , and 35.6 hours in K_s . The effective seeing in the reduced images is approximately $0''.47$ in all bands. The depth (3σ) reached was 26.8 mag in J_s , 26.2 mag in H , and 26.2 mag in K_s for point sources. All magnitudes in this paper are given in the AB system unless stated explicitly otherwise. Some examples of galaxies in these ultra-deep images are presented in Fig. 1. Combining these near infrared data with deep optical HST/WFPC2 imaging (version

⁷The size properties of galaxies in the MS1054-03 FIRES field (Förster Schreiber et al. in preparation) will be discussed in a forthcoming paper.

⁸The catalog and reduced images are available at <http://www.strw.leidenuniv.nl/~fires>

⁹The ISAAC pixel scale is actually $0''.147$, however we resampled the ISAAC pixels to 3×3 blocked HDF-S WFPC2 pixels.

2; Casertano et al. 2000), we assembled a K_s -selected catalogue containing 833 sources, of which 624 have seven-band photometry, covering $0.3\text{--}2.2\mu\text{m}$. Stars were identified, and removed from the catalog, if their spectral energy distributions (SEDs) were better fitted by a single stellar template than by a linear combination of galaxy templates. Four of the stellar candidates from this color classification were obviously extended and were reidentified as galaxies. Two bright stars were not identified by their colors because they are saturated in the HST images and were added to the list by hand. Photometric redshifts were estimated for the catalogued galaxies following Rudnick et al. (2001) (see also Section 3).

The sample of galaxies is selected in the K_s -band. For $z \lesssim 3$ this filter reflects galaxy flux at wavelengths redward than the rest-frame V-band and so selects galaxies in a way that is less sensitive to their current unobscured star formation rate than selection in the rest-frame UV. To select galaxies with reliable photometry, we exclude the much less exposed borders of our combined K_s “dithered” image (see Labbé et al. 2003), taking only those galaxies whose fractional exposure time is $\geq 35\%$ of the maximum. To ensure sufficient signal-to-noise for the subsequent size determinations, we limit ourselves to the 171 objects with $K_s \leq 23.5$ and with ISAAC and WFPC2 coverage.

2.2. Measuring sizes

The multiband imaging allows us to make a homogeneous comparison of the rest-frame optical size for all sample galaxies at redshift $z \lesssim 3$. We measure the sizes of galaxies at all redshifts consistently by fitting the profile of each galaxy in the band-pass which corresponds most closely to the rest-frame V-band at that redshift: for $0 < z < 0.8$ we fit the I_{814} -band, for $0.8 < z < 1.5$ the J_s -band, for $1.5 < z < 2.6$ the H-band, and for $2.6 < z < 3.2$ the K_s -band.

At high redshift the angular sizes of typical galaxies in our sample are comparable to the size of the seeing ($\sim 0''.47$). Consequently, the intrinsic structure and size of the galaxies must be obtained by adopting a surface brightness (SB) model and convolving it with the image PSF. This approach is well tested and successful at fitting low- z galaxies.

We seek a flexible parametric description of the galaxies’ SB distribution, without resorting to multi-component models. The population of galaxies at any redshift is likely a mixture of spirals, ellipticals and irregular objects. Elliptical galaxies (from dwarfs to cDs) are well fitted by a Sérsic model $r^{1/n}$ (Sérsic 1968), as demonstrated by a number of authors (see e.g. Trujillo, Graham & Caon 2001 and references therein). The Sérsic model is given by:

$$I(r) = I(0) \exp^{-b_n(r/r_e)^{1/n}}, \quad (1)$$

where $I(0)$ is the central intensity and r_e the effective radius, enclosing half of the flux from the model light profile. The quantity b_n is a function of the radial shape parameter n – which defines the global curvature in the luminosity profile – and is obtained by solving the expression $\Gamma(2n)=2\gamma(2n, b_n)$, where $\Gamma(a)$ and $\gamma(a, x)$ are respectively the gamma function and the incomplete gamma function.

The disks of spiral galaxies are also well described by a Sérsic model with $n=1$, corresponding to an exponential profile. The Sérsic model (with its free shape parameter n) is flexible enough to fit the radial profiles of nearly every galaxy type¹⁰. For this reason and for its simplicity, we decided to use it for measuring the sizes of galaxies in our data.

Both the intrinsic ellipticities of the galaxies and the effects of the seeing on the images were taken into account when fitting the model. Details of the particular model fitting method are given in Trujillo et al. (2001) and Aguerri & Trujillo (2002).

We start by measuring the SB and ellipticity profiles along the major radial axis by fitting isophotal ellipses to the sample object images, using the task ELLIPSE within IRAF¹¹. The fits extend down to 1.5 times the standard deviation of the sky background of the images. Some examples of the model fits to our sample galaxies are presented in Fig. 2. A Levenberg–Marquardt non–linear fitting algorithm (Press et al. 1992) was used to determine the set of free parameters which minimizes χ^2 . To do this, we fit simultaneously the observed 1D and ellipticity profiles using a PSF convolved model for each. In what follows, we refer to the *circularized effective radius* of the fitted model, i.e. $r_e = a_e \sqrt{(1 - \epsilon)}$, as the *size* of the galaxies; here a_e is the semi–major effective radius and ϵ the projected ellipticity of the galaxy model. We checked that the estimate of the intrinsic ellipticity of our sources, and hence the conversion to circularized effective radius, was not systematically affected by the seeing, by searching for trends with z or the K_s apparent magnitude (Fig. 3). No significant trends were found.

The PSF was estimated for every band by fitting a Moffat function to star profiles. We find the following β and FWHM (Full at Width Half Maximum) as our best fitting stellar parameters: $\beta=2.5$, FWHM=0".147 (I_{814} –band); $\beta=3$, FWHM=0".46 (J_s –band); $\beta=3$, FWHM=0".49 (H–band), and $\beta=3$, FWHM=0".47 (K_s –band). When fitting objects close to the resolution limit, it is crucial to have an accurate measure of the PSF. To test the robustness of our size measurements against slight errors in our PSF determination we compared

¹⁰Even early–type spirals composed by a bulge plus a disk can be fitted by a single Sérsic model (Saglia et al. 1997).

¹¹IRAF is distributed by the National Optical Astronomical Observatories, which are operated by AURA, Inc. under contract to the NSF.

our sizes to those determined using a completely independent fitting algorithm (GALFIT; Peng et al. 2002). This code uses the 2D profiles of the stars themselves to convolve the models with the seeing. In Fig. 4 we show the relative error between the size estimates using both our code and GALFIT. The difference between the sizes does not show any clear trend with z or the apparent K_s magnitude. The agreement between these two different algorithms ($\sim 68\%$ of the galaxies have a size difference less than 35%) corroborates the robustness of the size determination. One reason for this is that our very deep NIR data allows us to sample the profiles out to approximately 2 effective radii, providing ample constraints for the fit. For the smallest objects, our bright total magnitude limit ($K_s=23.5$) has the effect that the measured SB profile extends over 5 magnitudes and is therefore very well characterized. The size errors of each galaxy are taken into account in the subsequent analysis.

There are 3 galaxies where the size estimation is ill defined because they have a close companion. These galaxies represent only $\sim 1.5\%$ of the total and are all at $z < 1.15$. The final sample is composed of 168 galaxies. The sizes of these galaxies are shown in Table 1.

One way to test the quality of our model fits is to compare the model magnitude with an aperture isophotal magnitude (Labbé et al. 2003) (see Fig. 5). The total luminosity, L_T , associated with an $r^{1/n}$ profile extended to infinity can be written as

$$L_T = I(0)r_e^2 \frac{2\pi n}{b_n^{2n}} \Gamma(2n) \quad (2)$$

As expected for an extrapolation to infinity, the total model magnitude is almost always equal or brighter than the model-independent determination. In general, there is relatively good agreement between the two measures: a magnitude difference < 0.2 mag for 75% of the sample. The difference between the two estimators is largest for objects with the highest n values, as expected because of the large amounts of light at large radii in these models (Trujillo, Graham & Caon, 2001). Galaxies, however, certainly do not extend to infinity and the model extrapolation is likely unphysical, especially for high- n values. For this reason we choose the total luminosity from Labbé et al. (2003) in the following analysis.

3. THE OBSERVED LUMINOSITY/MASS VS SIZE RELATIONS AT HIGH-Z

We now present the relations between stellar luminosity, or stellar mass, and the rest-frame V-band size over a wide range of redshift. Throughout, we will assume $\Omega_M=0.3$, $\Omega_\Lambda=0.7$ and $H_0=100h$ km s $^{-1}$ Mpc $^{-1}$. We convert our measured angular sizes to physical

sizes using the photometric redshift determined for each object¹². These redshifts, and the rest-frame optical luminosities, were estimated by fitting a linear combination of nearby galaxy SEDs and model spectra to the observed flux points (Rudnick et al. 2001, 2003a). The accuracy derived from 39 available spectroscopic redshifts is very good, with $|z_{phot} - z_{spec}|/(1 + z_{spec}) \approx 0.05$ for $z > 1.4$. A plot of the z_{spec} versus z_{phot} for the present sample is shown in Labbé et al. (2003; Figure 6). We neglect the photometric redshift uncertainties in our analysis since a redshift error of even ± 0.5 at $z = 1.5$ correspond to size errors of $\lesssim 5\%$. On the other hand, our photometric redshift uncertainties equate to $\lesssim 35\%$ luminosity errors. For a first analysis step, we have split our sample into a $z \leq 1.5$ and a $z > 1.5$ bin and plot the rest-frame optical effective radius (the size estimated in the rest-frame band filter) versus the total luminosity in the rest-frame V-band in Fig. 6.

We also have explored the relation between stellar mass and size for our sample (see Fig. 6). The stellar mass-to-light ratios (M/L) and hence stellar masses for the individual galaxies were estimated by Rudnick et al. (2003b) from their rest-frame colors and SEDs, using a technique similar to that of Bell & de Jong (2001). Briefly, this approach exploits the relation between color and stellar mass-to-light ratio (M/L), which exists over a wide range of monotonic star formation histories, and which is rather robust against the effects of age, dust extinction, or metallicity. Errors in the derived masses will occur in the presence of bursts. In practice, we derive the M/L from the rest-frame $(B - V)$ color using the models presented in Bell & de Jong (2001). We take into account the photometric redshift probability distribution and the scatter in the $(B - V) - M/L$ relation when calculating our uncertainties (Rudnick et al. 2003b).

3.1. Selection Effects

For studying galaxy size evolution from Fig. 6, we must understand the selection effects at play in our sample. Redshift-dependent observational biases can mimic real evolutionary changes in the galaxy population, both through biases in the selection of galaxies and through the measurement of their sizes. Knowing the selection effects is also crucial in creating mock high redshift catalogs from low redshift surveys.

For a given flux limit (in our case $K_s=23.5$) there is a corresponding threshold in the rest-frame luminosity, which increases with redshift. This is well illustrated in the L_V-z diagram (Fig. 7) and demonstrates that our high- z sample represents only the most luminous fraction

¹²For 25% of the galaxies in our sample z was determined spectroscopically. When a z_{spec} determination is available, this is the value used.

of the galaxy population. The absence of bright galaxies at low redshift is largely due to the small volume of the HDF-S over this redshift range.

The detectability of an object, however, depends not only on its apparent magnitude, but also on its morphology and mean SB: for a given apparent magnitude, very extended, and hence low-SB, objects will have a lower signal-to-noise than a compact source. In practice, any image presents a SB limit beyond which the sample will be incomplete. For a given flux limit, the SB limit translates, therefore, into an upper limit on the size for which an object can still be detected. To determine the completeness of the FIRES K-band image we created 100,000 artificial galaxies with intrinsic exponential profiles and with structural parameter values covering the ranges $18 < K_s < 24$, $0''.03 < r_e < 3''.0$ and $0^\circ < i < 90^\circ$ ¹³. The model images were randomly placed, 20 at a time, into the K_s-band image, and SExtractor was run using the same parameters that were used to detect the real galaxies. Fig. 8 shows the fraction of galaxies successfully detected by SExtractor at each input value (K_s , r_e). Superimposed in Fig. 8, we show the K_s-band size and apparent magnitude for our sample objects. Also shown are lines of constant central SB for exponential models ($n=1$). Even for the conservative assumption of an exponential profile, we are complete over almost the entire range spanned by our sample galaxies. This can be understood simply because our NIR images are so deep. Our sample selection threshold is ~ 3 magnitudes brighter than the 3-sigma detection limit.

The exact SB limit for real distributions of galaxies is more complex, as galaxies have a range of profile shapes, with different Sérsic indices n and hence different central SBs. Indeed, the data show no clearly defined threshold. Nonetheless, as a conservative estimate of our completeness limit we adopt a threshold at a central SB of $\mu_K(0)=23.5$ mag/arcsec², for which we are 90% complete for an exponential model. Objects with this $\mu_K(0)$ that are more concentrated than an exponential would be detected with even more completeness than 90%. We have also found that, at the SB limit, we can retrieve the sizes to within $\sim 20\%$ of objects with $n=1$. However, for exponential objects near our SB limit, we underestimate the magnitude by a median of 0.25 mag (and >0.4 mag for 25% of these objects). This has to do with the way SExtractor measures magnitudes, which depends on apparent SB. We have also checked for possible incompleteness effects around the observed $K_s=23.5$ magnitude limit, because of small systematic underestimates of measured magnitudes, but find that they are

¹³Galaxies with values of n bigger than 1 are more centrally concentrated than an exponential and, hence, are easier to detect at a given total magnitude. Therefore, our choice of $n = 1$ is a conservative one. We do note, however, that objects with $n < 1$ will be harder to detect at a given total magnitude; such objects are found to be dwarf (faint) galaxies in the local universe and we assume that they will not be observed in our high- z sample.

not significant. The corrections to total magnitudes for observed galaxies near the SB limit are, however, uncertain. To be conservative we choose not to correct the flux at the SB limit and note that the application of any correction for missed flux would simply increased the derived luminosities of our galaxies.

In Fig. 9 we show how our conservative SB limit translates into the 90% completeness track in parameter plane of r_e and $L_{V,rest}$. For a given redshift, we are less than 90% complete for exponential galaxies with an effective radius larger than the corresponding line in Fig. 9. Due to $(1+z)^4$ SB dimming, redshift plays a very large role in this detectability. Similarly, for a given luminosity the maximal disk size to which we are complete will decrease with increasing redshift.

4. ANALYSIS

The selection effects will affect the distribution of points in Fig. 6 and make it impossible to read-off any size evolution, or lack thereof, without careful modelling. We explore evolutionary trends in the distribution of the galaxies in the above diagrams, by taking a $z=0$ luminosity-size (and mass-size) relation and by drawing a mock high redshift catalogs from these relations, subject to the redshift-dependent selection effects.

4.1. Simulating the local luminosity/mass vs. size relations at high redshifts

The Sloan Digital Sky Survey (SDSS, York et al. 2000) is providing an unprecedented database of $\sim 10^6$ nearby galaxies with spectroscopic redshifts and multi-band photometry. In particular, it has been used to derive the size distribution of present-epoch galaxies versus their luminosities and stellar masses (Shen et al. 2003). Shen et al. show the median and dispersion of the distribution of Sérsic half-light radius (Blanton et al. 2003) for different bands as a function of the luminosity and of the stellar mass. We have used their g-band (the closest available filter to our V-band) size distributions (S. Shen, 2003, private communication) as a local reference of the size distribution of galaxies in the nearby universe. We note that whereas Shen et al. show separately the distribution of early and late-type galaxies, we use their combination of these two subsamples into one, to make a direct comparison with our sample. For nearby galaxies of a given luminosity, Shen et al. propose the following size log-normal distribution with median \bar{r}_e and logarithmic dispersion σ :

$$f(r_e|\bar{r}_e(L), \sigma(L)) = \frac{1}{\sqrt{2\pi}\sigma(L)} e^{-\frac{\ln^2(r_e/\bar{r}_e(L))}{2\sigma^2(L)}} \frac{dr_e}{r_e}, \quad (3)$$

illustrated in Fig. 10.

The SDSS relations are used to test the null hypothesis, i.e., that the luminosity–size or mass–size relations do not change with redshift. It is important to note that this does not imply that the galaxies themselves do not change; they could certainly evolve ‘along’ such a relation. To test the null hypothesis, we construct distributions of SDSS galaxies as they would be observed at high redshift, mimicking our observations as follows: every simulated distribution of galaxies contains the same number of objects than our FIRES sample (i.e. 168). We pick a luminosity and redshift pairs at random from our observed sample. For this luminosity L , we evaluate a size at random from the local size sample distribution provided by the SDSS data (Eq. 3), by solving the following implicit equation:

$$F(r_e|L) = \frac{1}{2} \left\{ 1 - \Phi \left(\frac{\ln(r_e/\bar{r}_e(L))}{\sqrt{2}\sigma(L)} \right) \right\}; \quad (4)$$

where Φ is the error function and $F(r_e|L)$ is randomly distributed in $[0,1]$.

For every effective radius drawn from Eq. 4 we analyze if this galaxy (characterized by r_e , L , z) would be observed within the completeness limit of Fig. 9. If it is larger, it is not taken into account in our simulated distribution. The process for selecting a new galaxy is repeated until we have a mock sample with the same number of objects as galaxies observed.

This procedure assures that the simulated galaxy distribution follows the same redshift and luminosity distribution as the observed sample and also is affected by the same selection effects. An analogous procedure is repeated in the case of the size–mass relation replacing L with M_\star in Eqs. 3 and 4¹⁴. At this time, to account for the selection effects, we select a (M/L , L , z) triplet at random from the observed distribution.

Fig. 11 shows an example of how the SDSS galaxies would be distributed in the size diagrams with the same luminosity, mass and redshift distribution as the galaxies observed in FIRES. A comparison of Fig. 6 and 11 shows that the simulated SDSS data have a luminosity–size and a mass–size relation that is tighter than the observed FIRES relations. If the luminosity–size relation from SDSS remained unchanged with increasing z , we would

¹⁴Shen et al. use also a log–normal distribution for the size–mass relation. Their mass evaluation rests in the Kroupa (2001) IMF (Initial Mass Function). The stellar mass modelling of the FIRES data, however, uses a Salpeter IMF. In our simulations we have followed the procedures suggested in Kauffmann et al. (2003) of using $\text{Mass}_{IMF,Salpeter} = 2 \times \text{Mass}_{IMF,Kroupa}$ to transform from SDSS data to our data.

not expect to find small and luminous objects at high redshift, however these objects are present in the FIRES observations (see Fig. 6).

To quantify if these qualitative differences between the observed distributions and the simulated null hypothesis are significant, we ran the generalization of the Kolmogorov–Smirnov (K–S) test to two–dimensional distributions (Fasano & Franceschini 1987). We create 1000 SDSS realizations (both for luminosity and mass). For all the simulations the rejection probability is bigger than 99.9%. Consequently, we conclude that neither the luminosity–size nor the mass–size observed relations satisfy the null hypothesis.

To account for measurement errors in the size estimates of the FIRES galaxies, we also create mock “FIRES” data point distributions. To create these distributions we randomly vary every observed effective radius using a normal distribution with standard deviation equal to the size error measured for each galaxy. We make 1000 mock “FIRES” and compare for each the rejection probability between the SDSS and the mock “FIRES” data. The rejection probability for all mock samples is again more than 99.9% in the luminosity and the mass relations. So, the intrinsic dispersion of our measurements are unable to explain the difference with the SDSS simulated data.

We also explored the sensibility of the adopted FIRES selection limits through simulations: we have evaluated the SDSS DF including different central SB limit ranging from 23 to no restrictions at all. We do not find any significant difference in our results. As we expected due to the depth of our images, uncertainties in the selection effects do not affect our analysis.

4.2. Testing the hypothesis of evolution

The no–evolution hypothesis, that the size relations for all galaxies are redshift independent, can be rejected both for the L_V – r_e and M_\star – r_e relations. To quantify and constrain the evolution of these relations with redshift, we need to devise an evolution model. In the absence of clear–cut theoretical predictions, we have resorted to a heuristic parameterization that draws on the observed local distribution. We have assumed that the log–normal size distribution (Eq. 3) applies at all redshifts, but with evolving parameters:

$$\bar{r}_e(L, z) = \bar{r}_e(L, 0)(1 + z)^{-\alpha} \quad (5)$$

$$\sigma(L, z) = \sigma(L, 0)(1 + z)^\beta. \quad (6)$$

Here, $\bar{r}_e(L, 0)$ and $\sigma(L, 0)$ are the median size and dispersion provided at $z=0$ by the Shen et al. (2003) data, and α and β describe the redshift evolution. Note that Eq. 5 and Eq 6

imply the same size evolution for all the galaxies independently of their luminosity. We also assume an analogous parameterization for the masses. Both for L_V-r_e and $M_\star-r_e$ we explore the ranges between $[-2,3]$ for α and between $[-2,2]$ for β .

As for the null hypothesis, we generate simulated galaxy distributions for every pair (α, β) and we ran K-S test between these simulations and the observed data. Neither for L_V-r_e nor for $M_\star-r_e$ could we produce evolutionary scenarios (α, β) whose distribution functions are in agreement with what we see in the FIRES data. However, one must bear in mind that not all the luminosities can be observed over the full redshift range (see Fig. 7). To understand better what possible evolution our data imply and to avoid luminosity dependent redshift ranges we decided to create more homogeneous subsamples by splitting our sample in three different luminosity (mass) bins. Both our luminosity–size and mass–size observed distributions have been divided in three luminosity (mass) bins as detailed in Table 2¹⁵. The splitting of our sample into these intervals avoids that low luminosity (mass) galaxies at low redshift dominate the results of our analysis. The mean redshifts for the low/intermediate/high luminosity (mass) bins are 1.0, 1.6 and 2.0, respectively. These different sets measure evolution in a different luminosity (mass) range and a different redshift range, and splitting them helps to make this clear.

We now can check whether the observed FIRES relations can be explained if the evolutionary parameters α and β depend on the luminosity (mass), and write out the new distribution function explicitly, combining Eqs. 5 and 6 with Eq. 3:

$$g(r_e|\bar{r}_e, \sigma, z) = \frac{1}{\sqrt{2\pi}\sigma} \frac{dr_e}{r_e} \frac{dz}{(1+z)^\beta} e^{-\frac{\ln^2(r_e/\bar{r}_e(1+z)^\alpha)}{2\sigma^2(1+z)^{2\beta}}} \quad (7)$$

The expression in Eq. 7 is a probability density and we use this to evaluate α and β using a Maximum Likelihood Method. For each luminosity/mass subsample we show in Fig. 12 the likelihood contours (1σ and 2σ) in the plane of α and β . We have also included as a reference the point $\alpha=0$ and $\beta=0$ which indicates the case of no–evolution at this plane. The top row shows the evolution of the size distribution at a given luminosity. The mean size at a given luminosity changes significantly for luminous galaxies: at $\langle L_V \rangle \sim 2 \times 10^{10} h^{-2} L_\odot$ galaxies were typically three times smaller at $z \sim 2.5$ than now, and 4 times smaller for $L_V > 3 \times 10^{10} h^{-2} L_\odot$. A luminosity independent model (α and β independent of L) is less likely

¹⁵The lowest luminosity (mass) galaxies with $L < 0.3 \times 10^{10} L_\odot$ ($M_\star < 0.3 \times 10^{10} M_\odot$) are not presented in this analysis. These galaxies have $z \lesssim 1$ and, consequently, the results coming from this subsample are largely affected by the cosmic variance associated with the small volume enclosed in the HDF-S over this redshift range.

than our luminosity dependent model, justifying our choice of three subsamples. For the sizes at a given stellar mass the picture is qualitatively different: there is no evidence for significant evolution of the r_e – M_* relation, except for the most massive bin, $M_* > 3 \times 10^{10} h^{-2} M_\odot$. At $\langle M_* \rangle \sim 2 \times 10^{10} h^{-2} M_\odot$ the relation may only have changed by 20% since $z \sim 2.5$. The implied size evolution at $z = 2.5$ in each luminosity (mass) bin is summarized in Table 2. Note that in all cases the evidence for an evolving scatter of the L_V, M_* – r_e relations is marginal.

In Fig. 13, we visualize these results in a different way: we show the ratio between the present epoch mean size for every luminosity (mass) bin and the expected mean size as a function of redshift using the α values derived from the FIRES data (i.e. we show $\bar{r}_e(L, z)/\bar{r}_e(L, 0) = (1+z)^{-\alpha}$). The same is done for the mass. This figure shows the region enclosed by the 1σ level confidence contours. The lines stop at the limiting redshift z' we are able to explore for the different luminosity (mass) bins.

Again, Fig. 13 shows that high- z galaxies (most luminous bin) at $z \sim 2.5$ are more compact (a factor of 4) than the nearby equally luminous galaxies. On the other hand, high- z galaxies differ only slightly in size at a given mass from the present-epoch. In the middle luminosity (mass) bin the evolution with z appears to be less important. For the L_V – r_e relations the dispersion of the high- z population increases in all the cases. This increase is, however, relatively moderate (a factor of 1.2–2.). We discuss how we can understand these results in the following section.

5. DISCUSSION

Using the observed nearby SDSS size relations (Shen et al. 2003) as the correct local references, the observed FIRES size–luminosity and mass–size distributions at high- z show a very different degree of evolution. The mass–size relation has remained practically unchanged whereas, the size–luminosity has evolved significantly: there are many more compact luminous objects at high- z than now. How can we re-concile these two observational facts?

In absence of M/L evolution with time, a change in the size–luminosity relation with z would imply the same degree of evolution in the mass–size relation. However, the mean M/L ratio decreases with increasing z . In the nearby universe, most galaxies have large M/L ratios (see Fig. 14 of Kauffmann et al. 2003). In contrast, FIRES galaxies at $z > 2$, at all luminosities, have M/L ratios of the order ~ 1 (Rudnick et al. 2003b). Consequently, although we observe a strong evolution in the luminosity–size relation, the decrease of M/L avoids a significant change in the observed mass–size relation.

We can therefore characterize our observed high- z galaxy population as follows: small to medium size objects (effective radius $\sim 1.5 h^{-1}$ kpc) not very massive ($\sim 3 \times 10^{10} h^{-2} M_{\odot}$) but often very luminous ($\sim 3 \times 10^{10} h^{-2} L_{\odot}$) in the V-band. The above picture does not mean that large galaxies can not be found at high z (Labbé et al. 2003b), but that they are relatively rare.

Traditionally the high- z population has been selected by the Lyman Break selection technique (Steidel & Hamilton 1993) known to select luminous unobscured star-forming galaxies. However, dust obscured or UV-faint galaxies may have been missed. The galaxies in FIRES are selected from very deep near infrared K_s -band imaging, and consequently, are expected to be less affected by this problem and give a more complete mass census of the high- z universe. In fact, the population of galaxies under study consists in part of a red population (Franx et al. 2003), which would be largely missed by the Lyman Break technique, but whose volume number density is estimated to be half that of LBGs at $z \sim 3$.

Hierarchical models for structure formation in a Λ dominated universe predict that LBGs have typical half-light radii of $\sim 2 h^{-1}$ kpc (Mo, Mao & White 1999) in good agreement to the size of the galaxies we are measuring and to the observed sizes for LBGs of other authors (Giavalisco, Steidel & Macchetto 1996, Lowenthal et al. 1997). Interestingly, other authors have observed LBGs using optical filters and, consequently, these sizes are UV sizes. The fact that their measures and ours (which are in the optical rest-frame) do not differ significantly could be evidence that the star formation of the LBGs is extended over the whole object¹⁶. In fact, if we select in our sample those galaxies with $L_V > 2 \times 10^{10} h^{-2} L_{\odot}$ and $z > 2.5$, 1/2 of this subsample would be considered as LBGs following the Madau et al. (1996) color criteria. We will explore the relation of UV and optical sizes in a forthcoming paper.

“High-redshift disks are predicted to be small and dense, and could plausibly merge together to form the observed population of elliptical galaxies” (Mo, Mau & White 1998). We have made a simplistic comparison between the above prediction and our data in Fig. 14. The lines represent the expected internal mass density M/r_e^3 of disks galaxies just formed at each redshift for three different values of the specific angular momentum. These lines are evaluated combining the Eqs. (4) and (12) of Mo et al. (1998) and assume a constant fraction of the mass of the halo which settles into the disk, $m_d = 0.05$, and a constant spin parameter of the halo $\lambda = 0.05$. With these two assumptions the internal mass density increases with z as the square of the Hubble constant $H(z)$.

Galaxies more massive than $10^{10} M_{\odot}$ are observable over the complete range in redshift.

¹⁶There is some evidence that the LBGs morphology depends not much on the wavelength, remaining essentially unchanged from the far-UV to the optical window (Giavalisco 2002 and references therein).

The measured mean internal density for this galaxy population appears to evolve only slightly with z , in agreement with the lack of strong evolution in the size–mass relation. If all the galaxies present in Fig. 14 were disks, their distribution would not be compatible with the theoretical expectation. However, we must take into account that we are observing a mix of galaxy types and not only disk galaxies. In order to address this point we have made a visual galaxy classification of all the objects with $z < 1.5$ and mass larger than $10^{10} M_{\odot}$. We can do that because of the high–resolution of the HST images in the I_{814} –band filter. This examination showed that the dense objects ($M/r_e^3 > 10^{10} M_{\odot}/\text{kpc}^3$) with $z < 1.5$ appear to be all ellipticals and that the late type fraction appears to increase as one moves to lower density objects. Unfortunately, we cannot make a similar analysis for $z > 1.5$ and the question of whether the high density objects we observe there are disk dominated remains unsolved. However, it is highly tempting to propose that our high z dense population could be the progenitors of the nearby dense elliptical galaxies.

Independently of the nature of the LBGs and of the red population it is clear that in order to reach the mass and sizes of the nearby galaxies an evolutionary process must be acting on the high– z population. Recently, Shen et al. have proposed, for the early–type galaxies, a simple model of mass and size evolution based on subsequent major mergers. This model explains the observed relations for these kind of galaxies between mass and size in the SDSS data, i.e. $R \propto M^{0.56}$. In the Shen et al. picture two galaxies with the same mass ($M_1 = M_2$) and radius ($R_1 = R_2$) merge forming a new galaxy with mass $M = 2M_1$ and radius $R = 2^{0.56} R_1$. If this process is repeated p times: $M = 2^p M_1$ and $R = 2^{0.56p} R_1$. If we take a galaxy at $z = 3$ (following our mass and size estimates) with $M_1 = 3 \times 10^{10} h^{-2} M_{\odot}$ and $R_1 = 1.5 h^{-1} \text{ kpc}$ this implies that after 3 major mergers $M = 24 \times 10^{10} h^{-2} M_{\odot}$ and $R = 4.8 h^{-1} \text{ kpc}$, in excellent agreement to the values we see in nearby galaxies ($M = 24 \times 10^{10} h^{-2} M_{\odot}$ and $R = 5 h^{-1} \text{ kpc}$, see Fig. 10). These numbers may suggest that the massive and dense high– z population can be understood as the progenitors of the bright and massive nearby early type galaxies.

6. SUMMARY

Using ultra–deep near–infrared images of the HDF–S we have analyzed the rest–frame optical band sizes of a sample of galaxies selected down to $K_s = 23.5$. This has allowed us to measure the evolution of the luminosity–size and mass–size relation out to $z \sim 3$. This is the first time that the rest–frame V–band sizes of such distant galaxies have been systematically analyzed as a function of stellar luminosity and stellar mass.

We compared our observed luminosity–size and mass–size relations to those measured in the nearby universe by the SDSS data (Shen et al. 2003). For this comparison we have

analyzed in detail the detectability effects that high- z observations impose on the observed relations. From this comparison, assuming the Shen et al. distributions are correct, we found:

1. The size–luminosity relation has evolved since $z \sim 2.5$. Luminous objects ($L_V \sim 3 \times 10^{10} h^{-2} L_\odot$) at $z \sim 2.5$ are 4 times smaller than equally luminous galaxies today.
2. The size–stellar mass relation has remained nearly constant since $z \sim 2.5$: for $\langle M_\star \rangle \sim 2 \times 10^{10} h^{-2} M_\odot$ the change is $20(\pm 20)\%$; for stellar masses larger than $3 \times 10^{10} h^{-2} M_\odot$ the characteristic mean size change is $40(\pm 15)\%$.

The above results are reconciled by the fact the M/L values of high- z galaxies are lower than nowadays $\langle M/L \rangle \sim 1$ (Rudnick et al. 2003b). Consequently, the brightest high- z galaxies are a group composed of a high internal luminosity density population but with a mean internal stellar mass density not much higher than found in the nearby universe. The observed small sizes of distant galaxies found here and in previous studies for LBGs (Giavalisco, Steidel & Macchetto 1996; Lowenthal et al. 1997; Ferguson et al. 2003) are in agreement with the small evolution of the mass–size relation because the typical masses of $z=3$ galaxies are substantially smaller than those at low redshift.

We are happy to thank Shiyin Shen for providing us with the Sloan Digital Sky Survey data used in this paper and Boris Häußler for running GALFIT. We thank the staff at ESO for the assistance in obtaining the FIRES data and the the Lorentz Center for its hospitality and support. We also thank the anonymous referee for useful comments.

Funding for the creation and distribution of the SDSS Archive has been provided by the Alfred P. Sloan Foundation, the Participating Institutions, the National Aeronautics and Space Administration, the National Science Foundation, the US Department of Energy, the Japanese Monbukagakusho, and the Max-Planck Society. The SDSS Web site is <http://www.sdss.org>. The SDSS is managed by the Astrophysical Research Consortium (ARC) for the Participating Institutions. The Participating Institutions are the University of Chicago, Fermilab, the Institute for Advanced Study, the Japan Participation Group, Johns Hopkins University, Los Alamos National Laboratory, the Max-Planck-Institut für Astronomie (MPIA), the Max-Planck-Institut für Astrophysik (MPA), New Mexico State University, University of Pittsburgh, Princeton University, the US Naval Observatory, and the University of Washington.

REFERENCES

- Aguerri, J.A.L. & Trujillo, I., 2002, MNRAS, 333, 633
- Avila-Reese, V & Firmani, C., 2001, RevMexAA, 10, 97
- Baugh, C. M., Cole, S., Frenk, C. S., & Lacey, C. G. 1998, ApJ, 498, 504
- Blanton, M. et al., 2003, ApJ, 592, 819
- Bell, E. F. & de Jong, R. S., 2001, ApJ, 550, 212
- Casertano, S., Ratnatunga, K. U., Griffiths, R. E., Im, M., Neuschaefer, L. W., Ostrander, E. J. & Windhorst, R. A., 1995, ApJ, 453, 599
- Casertano, S. et al. 2000, AJ, 122, 2205
- Franx, M. et al., "FIRES at the VLT: the Faint Infrared Extragalactic Survey", The Messenger 99, pp. 20–22, 2000
- Franx, M. et al., 2003, ApJL, 587, L79
- Fasano, G. & Franceschini, A., 1987, MNRAS, 225, 155
- Ferguson et al. 2003, ApJL, in press
- Giavalisco, M., Steidel C.C. & Macchetto, F.D., 1996, ApJ, 470, 189
- Giavalisco, M., 2002, ARA&A, 40, 579
- Kauffmann, G., et al., 2003, MNRAS, 341, 33
- Kroupa, P., 2001, MNRAS, 322, 231
- Labbé, I.F.L. et al., 2003, AJ, 125, 1107
- Labbé, I.F.L. et al., 2003b, ApJ, 591, L95
- Lilly, S. et al. 1998, ApJ, 500, 75
- Lowenthal, J.D., Koo, D.C., Guzmán, R., Gallego, J., Phillips, A.C., Faber, S.M., Vogt, N.P., Illingworth G.D., 1997, ApJ, 481, 67
- Madau, P., Ferguson, H.C., Dickinson, M.E., Giavalisco, M., Steidel, C.C. & Fruchter, A., 1996, MNRAS, 283, 1388
- Mao, S., Mo, H. J. & White, S.D.M., 1998, MNRAS, 297, L71
- Mo, H. J., Mao, S. & White, S.D.M., 1999, MNRAS, 304, 175
- Moorwood, A. F. 1997, Proc. SPIE, 2871, 1146
- Peng, C.Y., Ho, L.C., Impey, C.D. & Rix, H.W., 2002, AJ, 124, 266

- Press, W.H., Teukolsky, S.A., Vetterling, W.T. & Flannery, B.P., 1992, Numerical Recipes (Cambridge: Cambridge Univ. Press)
- Roche, N., Ratnatunga, K., Griffiths, R. E., Im, M. & Naim, A., 1998, MNRAS, 293, 157
- Rudnick, G. et al., 2001, AJ, 122, 2205
- Rudnick, G. et al., 2003a, ApJ, in press, astro-ph/0307149
- Rudnick, G. et al., 2003b, in preparation
- Saglia, R. P., Bertschinger, E., Baggle, G., Burstein, D., Colless, M., Davies, R. L., McMahon, R. K., Wegner, G. 1997, ApJS, 109, 79
- Sérsic, J.-L. 1968, Atlas de Galaxias Australes (Cordoba: Observatorio Astronomico)
- Shen, S., Mo, H.J., White, S.D.M., Blanton, M.R., Kauffmann, G., Voges, W., Brinkmann, J. & Csabai, I., MNRAS, 2003, 343, 978
- Smail, I., Hogg, D. W., Yan, L, Cohen, J. G., 1995, ApJ, 449, L105
- Somerville, R. S., Primack, J. R., & Faber, S. M. 2001, MNRAS, 320, 504
- Steidel, C.C. & Hamilton, D., 1993, AJ, 105, 2017
- Steidel C.C., Giavalisco, M., Pettini, M., Dickinson, M., & Adelberger, K. L., 1996, ApJ, 462, L17
- Trujillo, I., Aguerri, J.A.L., Gutiérrez, C.M., & Cepa, J., 2001, AJ, 122, 38
- Trujillo, I., Graham, A. W., & Caon, N., 2001, MNRAS, 326, 869
- York D. et al., 2000, AJ, 120, 1579

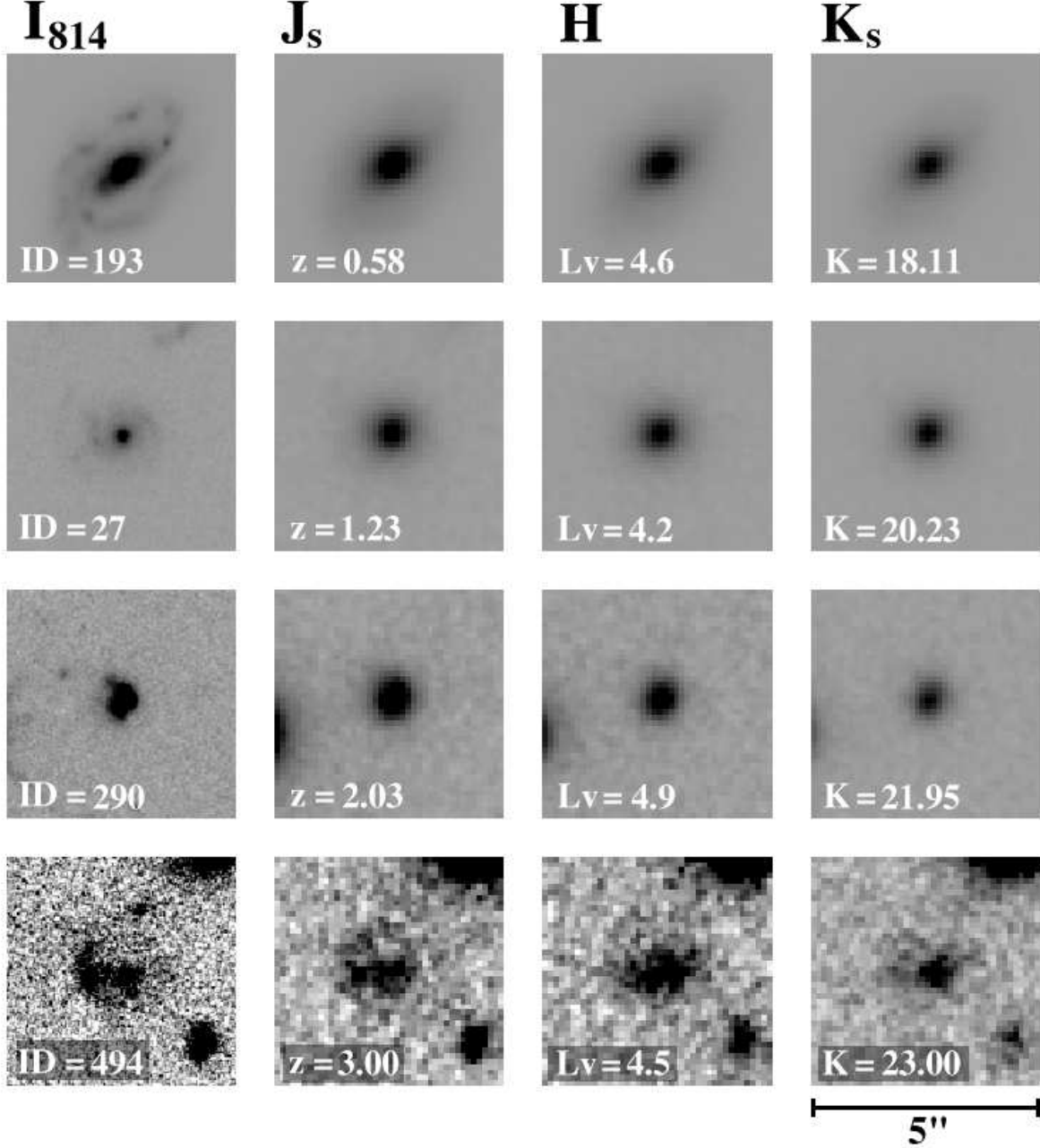


Fig. 1.— A mosaic of similar rest-frame V-band luminosities galaxies at different redshifts. The apparent K-band magnitude decreases towards the bottom. The luminosities are given in 10^{10} solar luminosities. The galaxies are shown in four different filters.

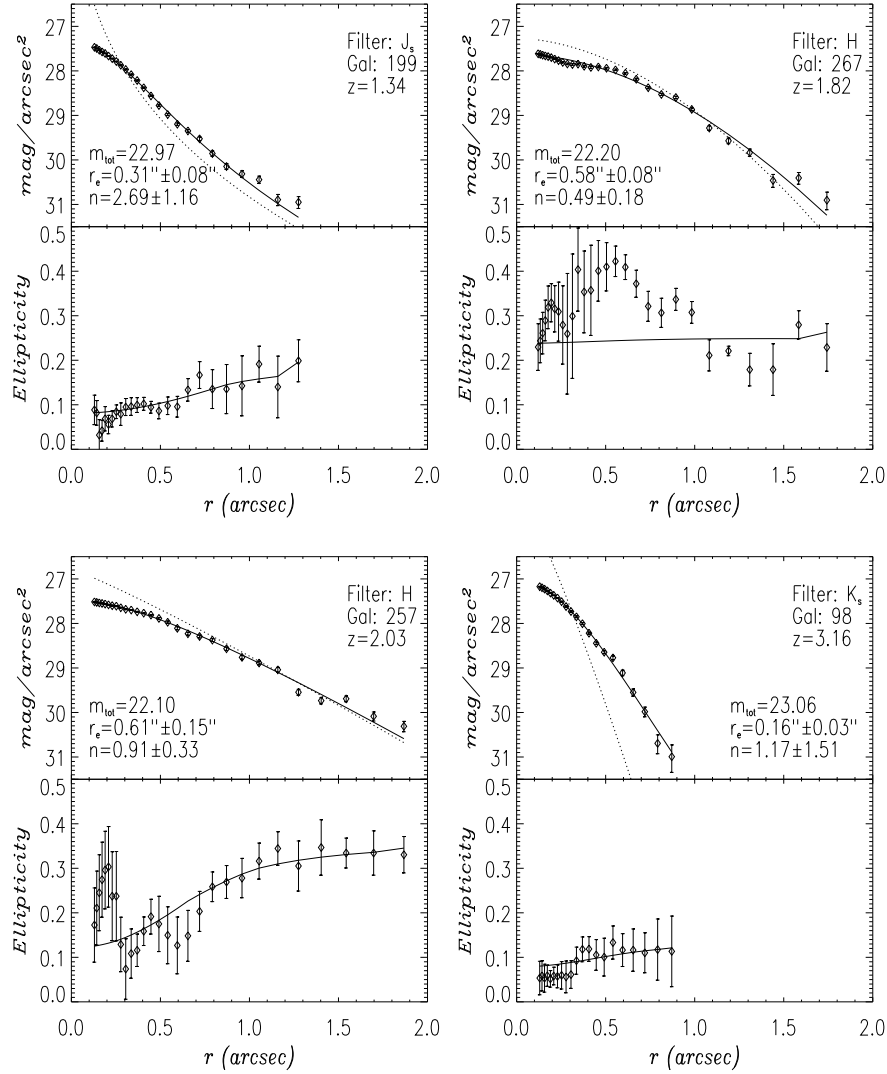


Fig. 2.— Surface brightness and ellipticity semi-major radial profiles fitting to four galaxies in our sample. Every galaxy is fitted in its optical rest-frame band following the criteria explained in the text. The galaxy identification numbers correspond to the catalog identification (see Labbé et al. (2003)). Superimposed on the surface brightness profile data are the model profile (dashed line) and the convolution of this model profile (solid line) to match the data. The solid lines in the ellipticity radial profiles show the fit to the ellipticities using our algorithm. Intrinsic ellipticities (i.e. not seeing convolved) of the galaxies can be obtained by extrapolating to infinity the solid lines. Details of the fitting algorithm can be found in Trujillo et al. (2001) and Aguerri & Trujillo (2002).

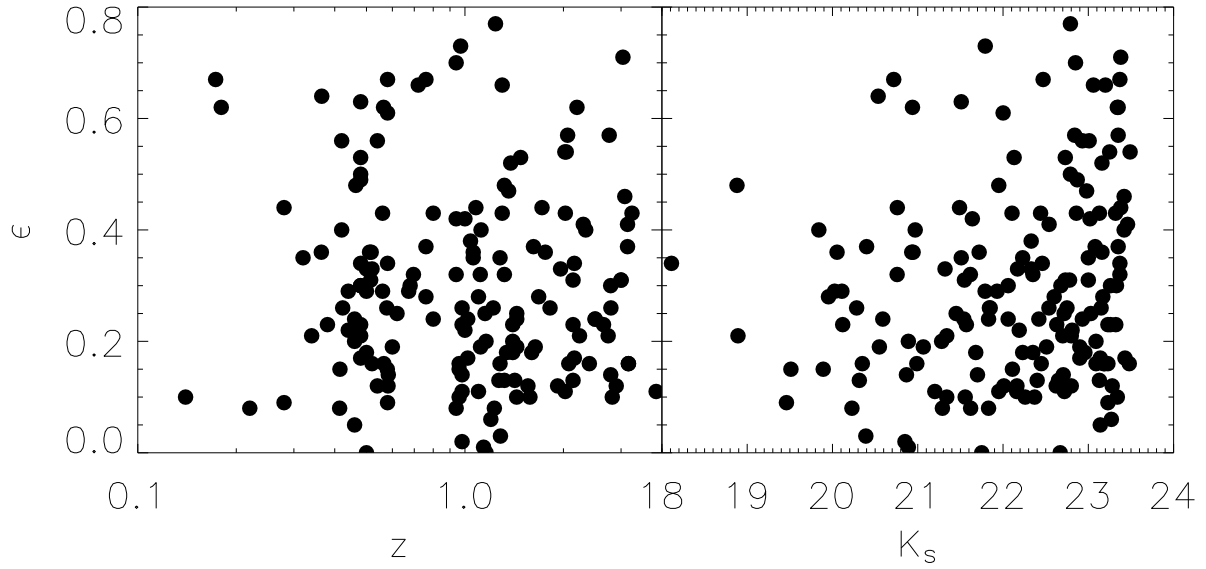


Fig. 3.— The intrinsic (i.e. the recovered non-seeing affected) ellipticity of the galaxies versus: a) the redshift of the observed sources and b) the apparent K_s total magnitudes. No clear relation is observed.

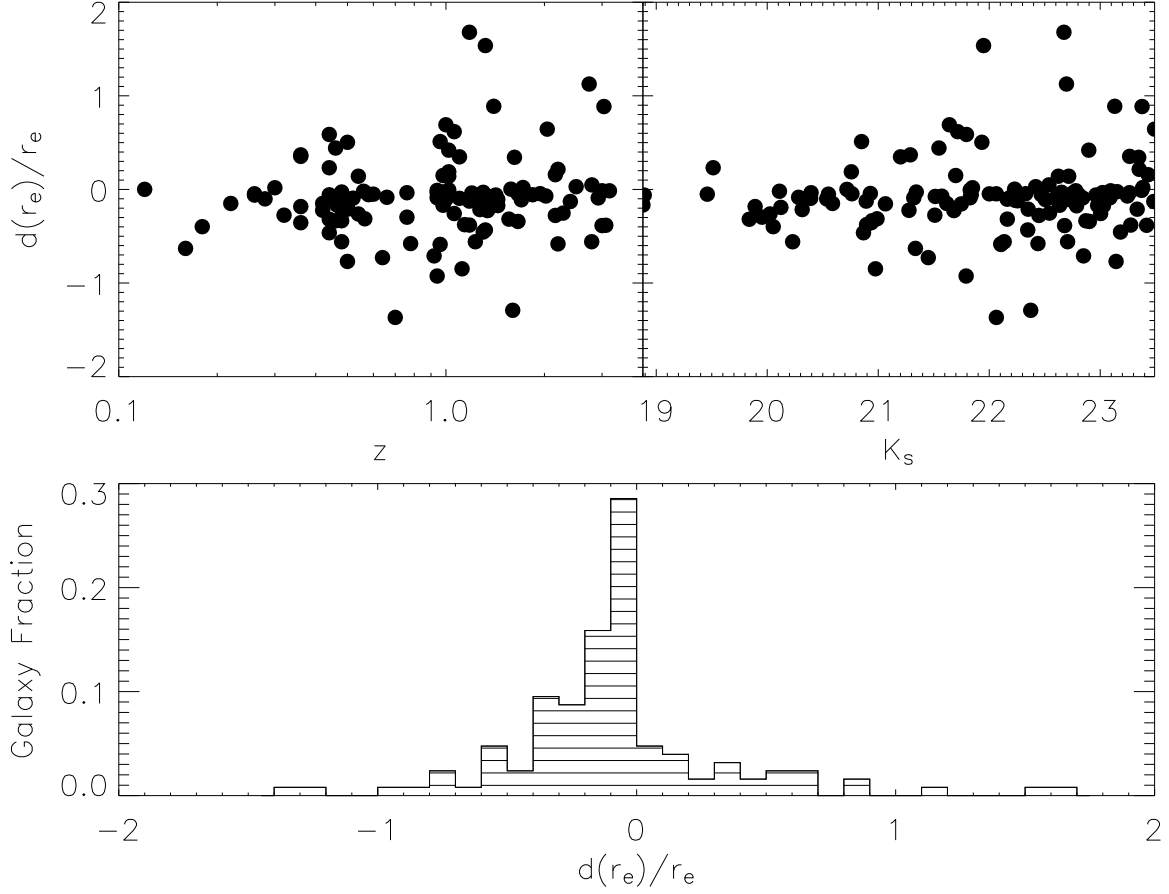


Fig. 4.— The relative error between the size estimation using our code and GALFIT $d(r_e)/r_e = 2 \times (r_e(\text{GALFIT}) - r_e(\text{ours})) / (r_e(\text{GALFIT}) + r_e(\text{ours}))$ is shown versus z and versus the apparent K_s magnitude. No clear trend is found. The histogram shows that for $\sim 68\%$ of the galaxies the difference is less than 35%.

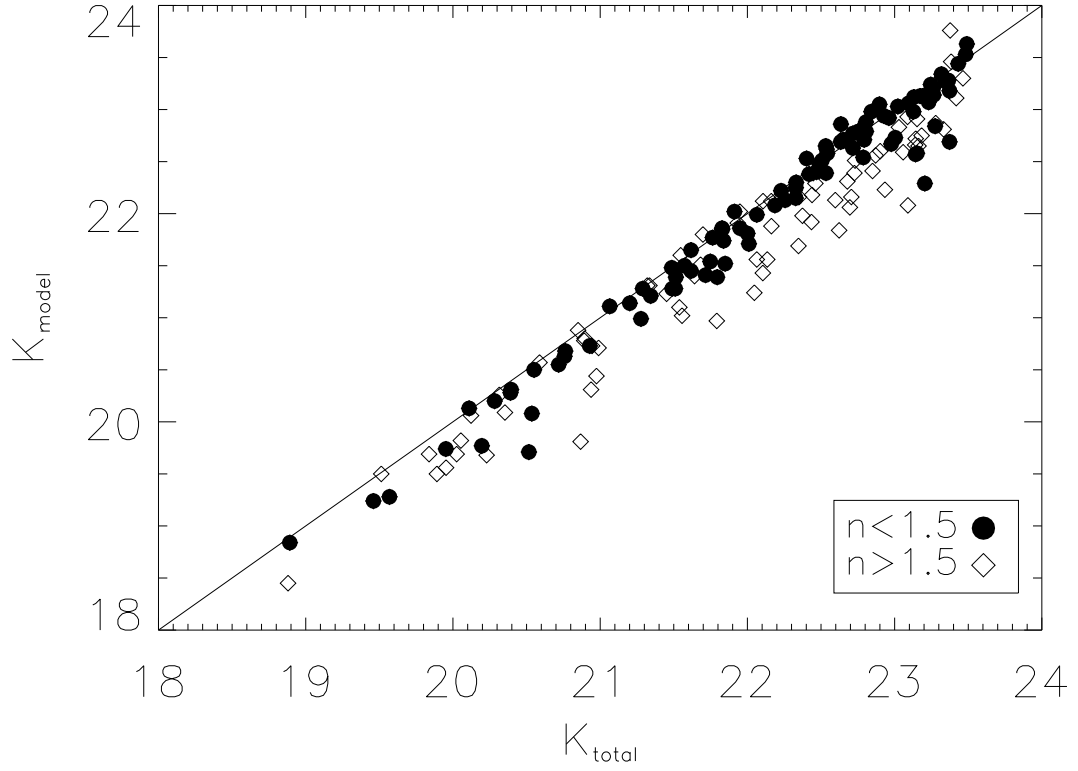


Fig. 5.— The total magnitude retrieved from the model fitting is compared to the total magnitude measured in a model independent way for the galaxies analyzed in this paper. Galaxies with $n < 1.5$ are represented with solid circles and galaxies with $n > 1.5$ with open diamonds.

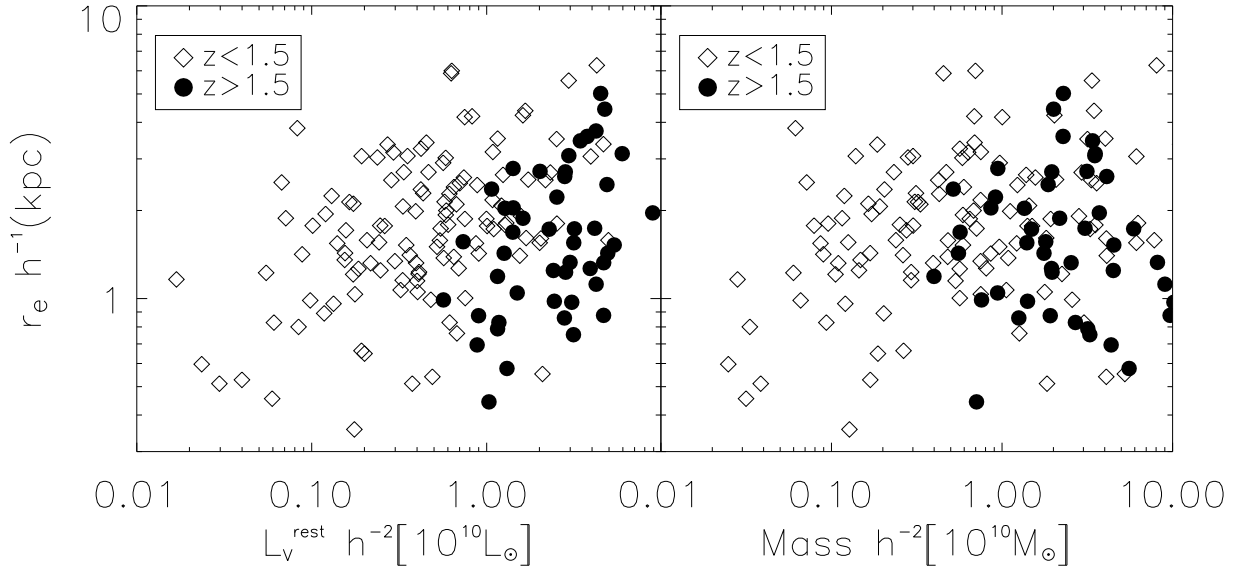


Fig. 6.— *Left*: The distribution of rest-frame optical sizes versus the rest-frame V-band luminosities is shown. Galaxies with redshifts smaller than 1.5 are represented with open diamonds and galaxies with redshifts bigger than 1.5 with solid circles. *Right*: Same as before but with the stellar mass. For clarity error bars are not shown. The mean size relative error is 35%.

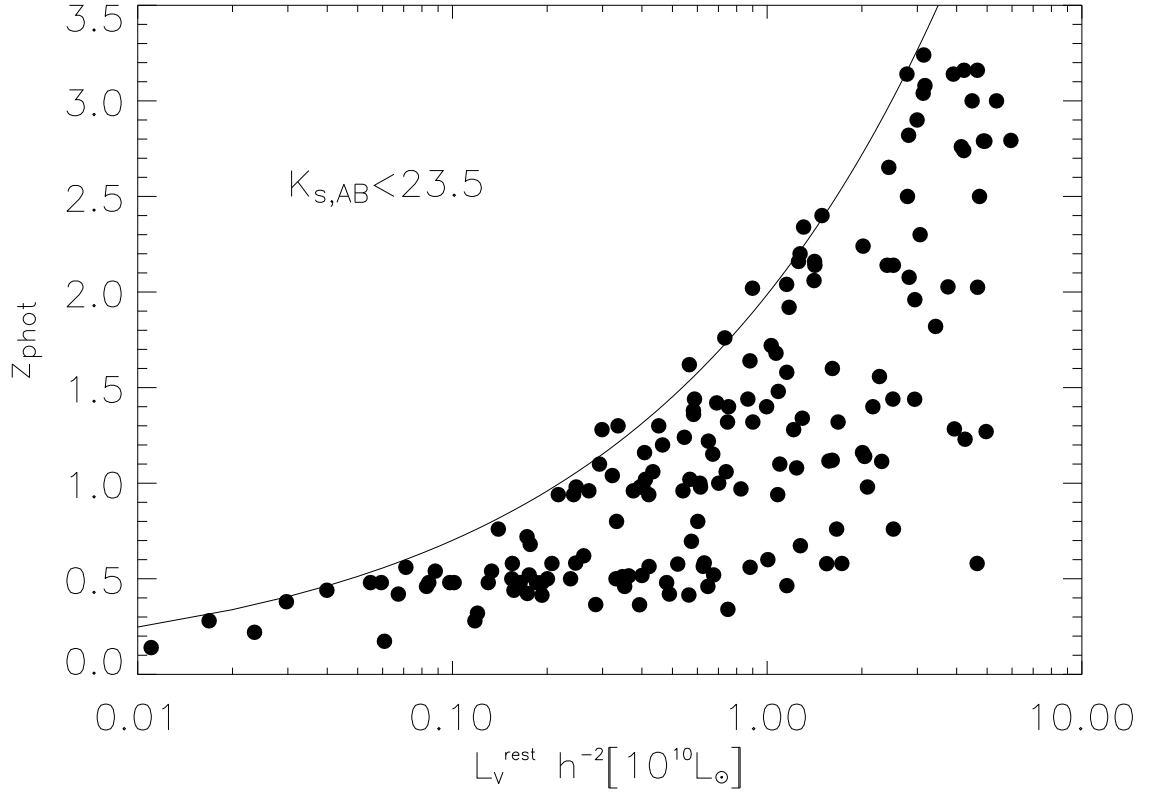


Fig. 7.— The L_V - z diagram for the objects selected in our sample with $K_s < 23.5$. The track represent the values of L_V^{rest} for a Scd template spectra (see Rudnick et al. (2001); Figure 11c) normalized at each redshift to $K_{s,AB}=23.5$.

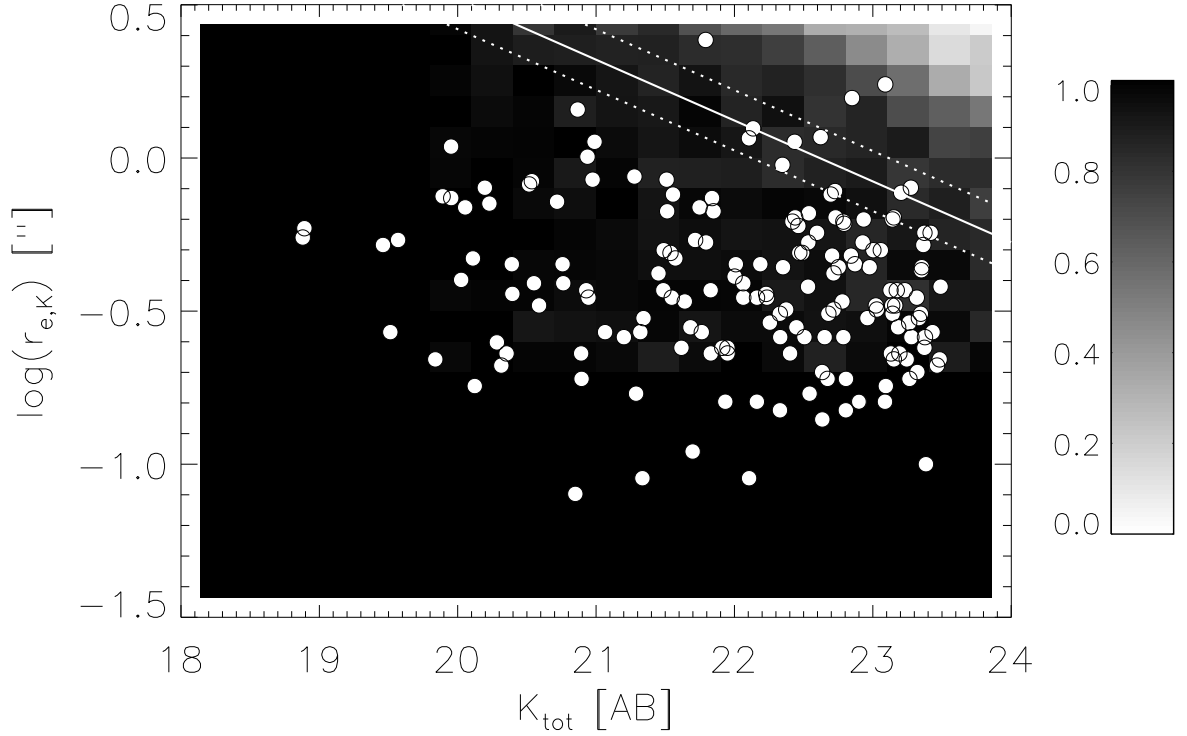


Fig. 8.— A completeness map for detecting galaxies with exponential profiles in the FIRES K-band data. The horizontal and vertical axis represent the input values. Overplotted is the K_s -band size versus the apparent K_s magnitude for the objects in our sample (open points). We have also shown exponential models ($n=1$) with central surface brightness of 23 and 24 mag/arcsec^2 (dotted lines). The solid line represents the central surface brightness ($\mu_K(0)=23.5 \text{ mag/arcsec}^2$) at which we are 90% complete.

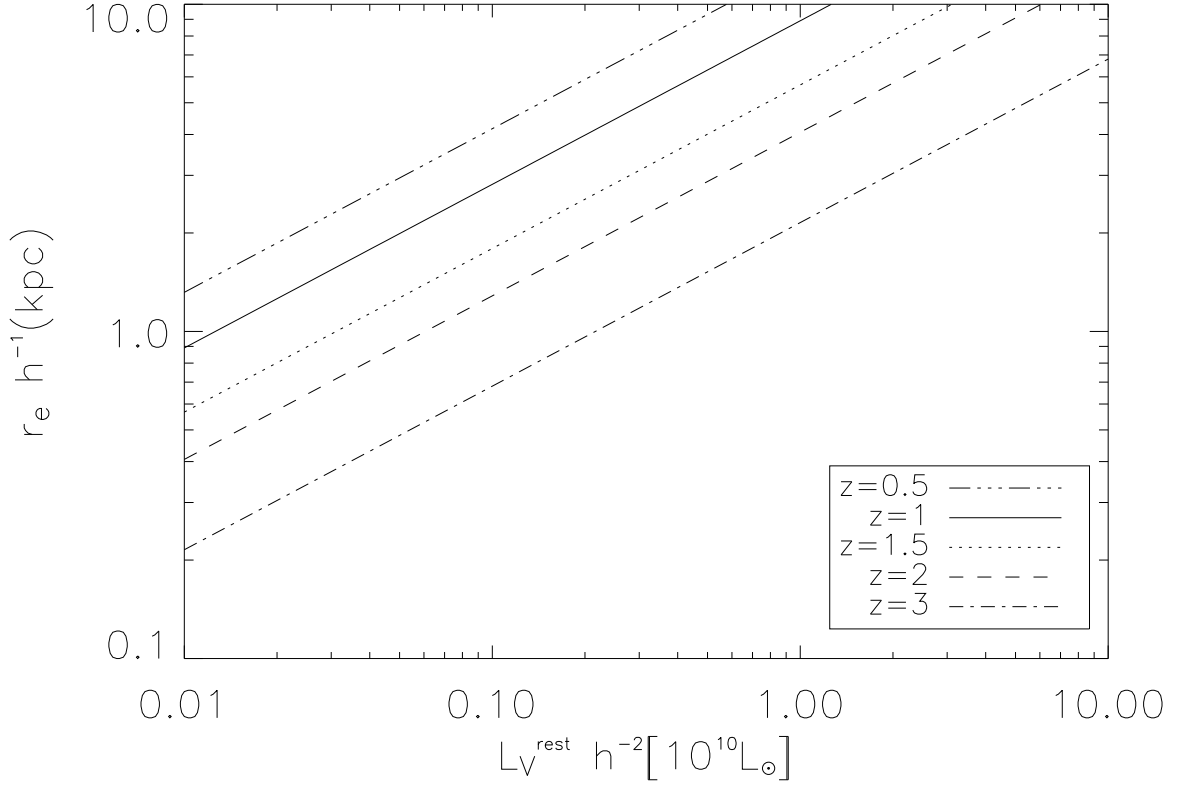


Fig. 9.— The 90% completeness tracks in effective radius for an exponential model with central surface brightness at K_s of $23.5 \text{ mag/arcsec}^2$ (see Fig. 8). We adopt these conservative limits when creating mock high redshift catalogs of SDSS galaxies. To convert from observed K-band magnitudes to rest-frame V-band luminosities we used an Scd template (see Fig. 11c from Rudnick et al. 2001).

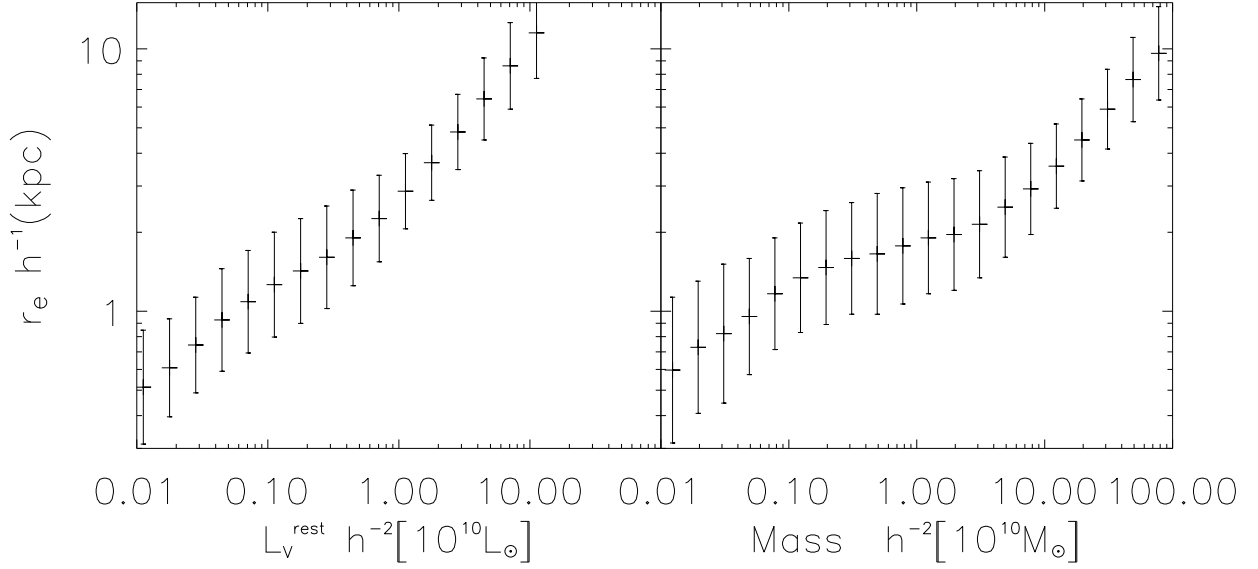


Fig. 10.— *Left*: The median and dispersion of the distribution of the Sérsic half-light radius of the SDSS galaxies (in the g-band) as a function of the g-band luminosity (the closest available filter to our V-band). *Right*: Same as before but as a function of the stellar mass. Note that the luminosity and the mass extends in this figure up to 10^{12} solar luminosities (masses).

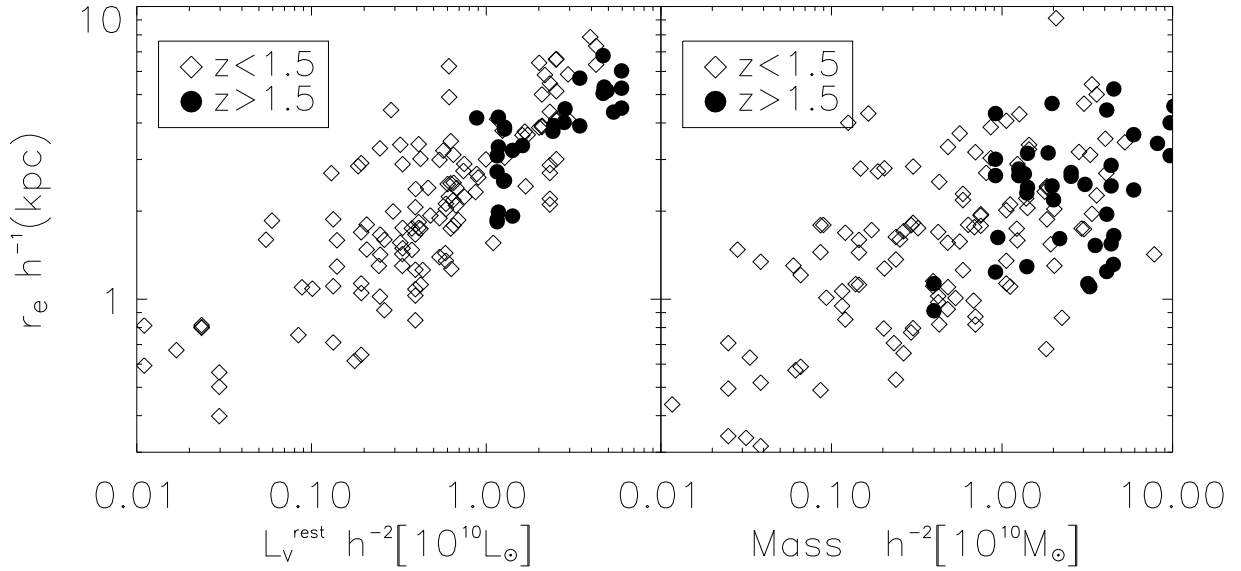


Fig. 11.— Predictions of the null hypothesis: *Left*: Simulated distribution of rest-frame optical sizes versus the rest-frame V-band luminosities for the SDSS data is shown (see text for details). Galaxies with redshifts smaller than 1.5 are represented with open diamonds and galaxies with redshifts bigger than 1.5 with solid circles. *Right*: Same as before but with the stellar mass.

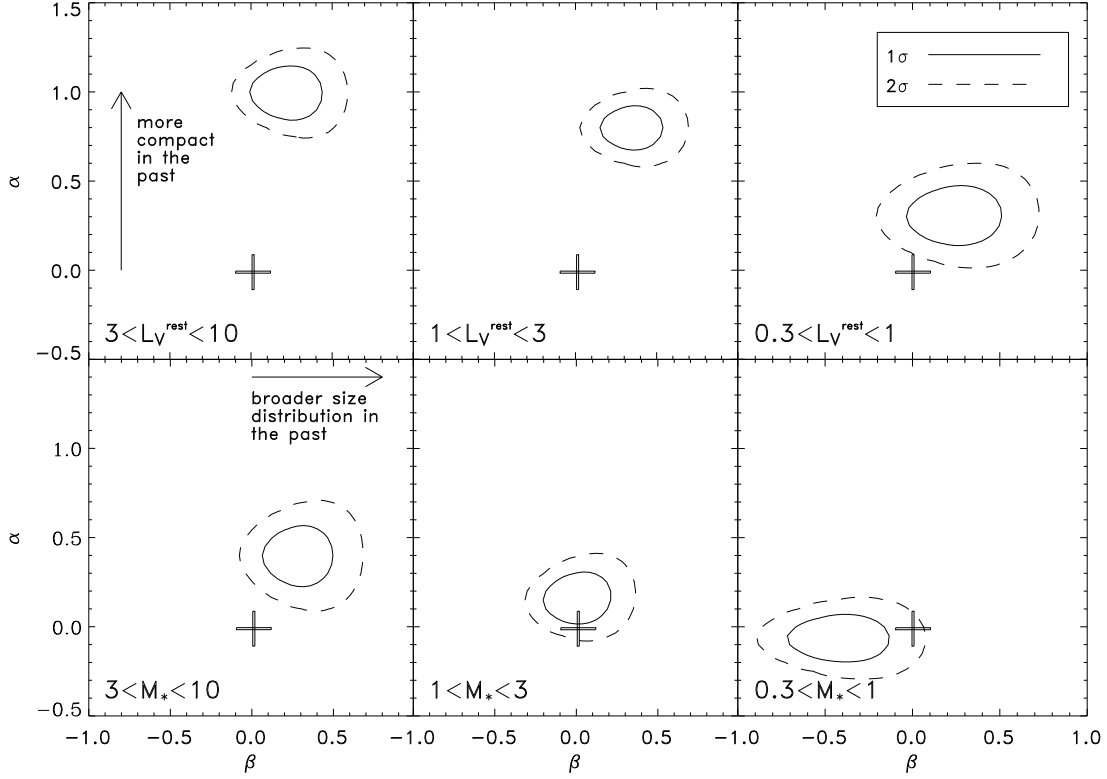


Fig. 12.— Likelihood contours representing the evolution in size and dispersion in the α - β plane. The top (bottom) row shows the evolution of the luminosity-size (mass-size) relation. Solid line represents the 1σ confidence level contour, dashed line the 2σ confidence level. The cross shows the position of no-evolution in this plane. Positive values of α represent decreasing values of the size with redshift. Positive values of β represent increasing the intrinsic dispersion σ of the population with redshift. Both the luminosity and the mass are in units of 10^{10} solar value. Both the no evolution model and a luminosity independent evolution model are less likely than the luminosity dependent model.

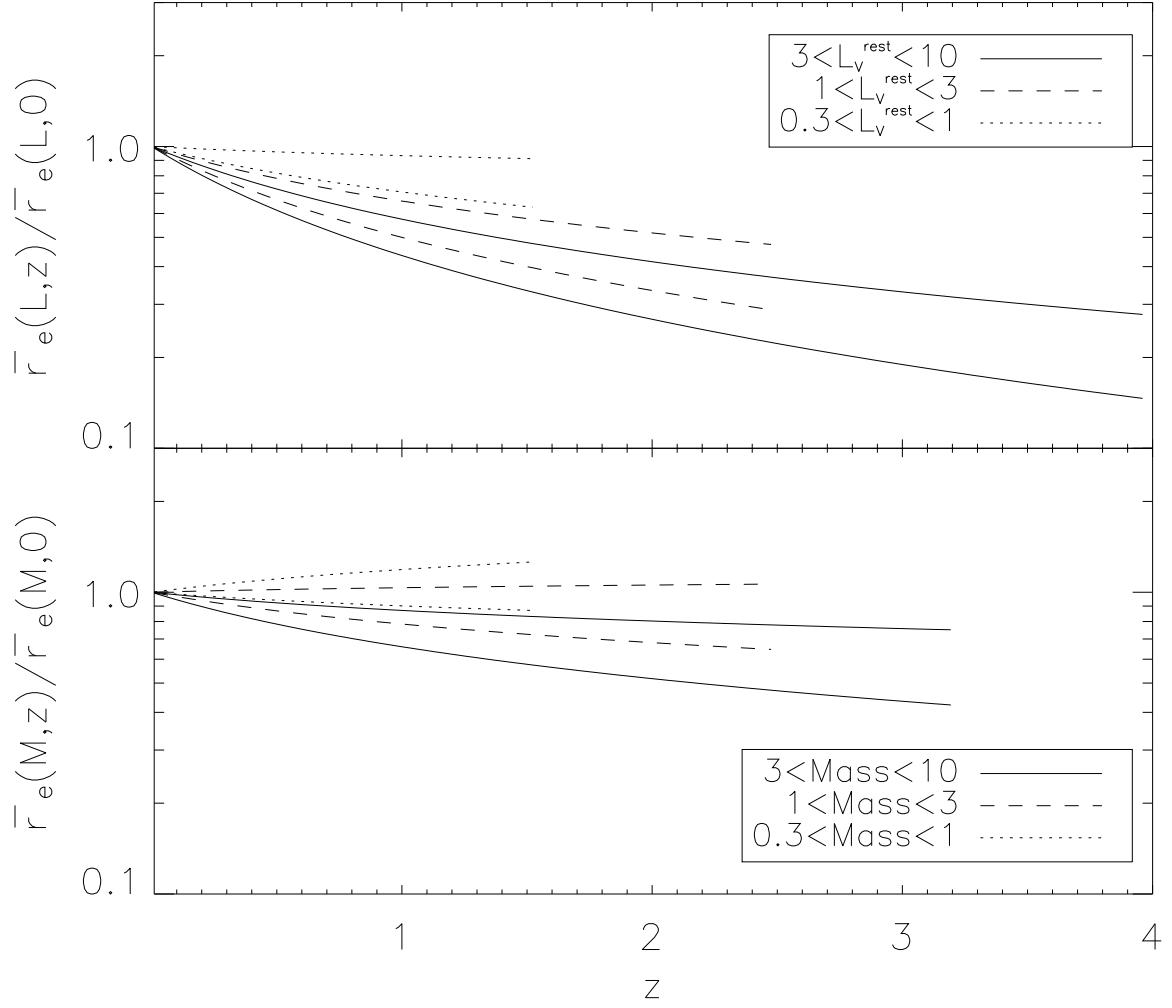


Fig. 13.— The ratio between the SDSS mean size and the expected mean size as a function of z is shown both for the luminosity and for mass relations. Both the luminosity and the mass are in units of 10^{10} solar value. Equal style lines enclose the 1σ variation.

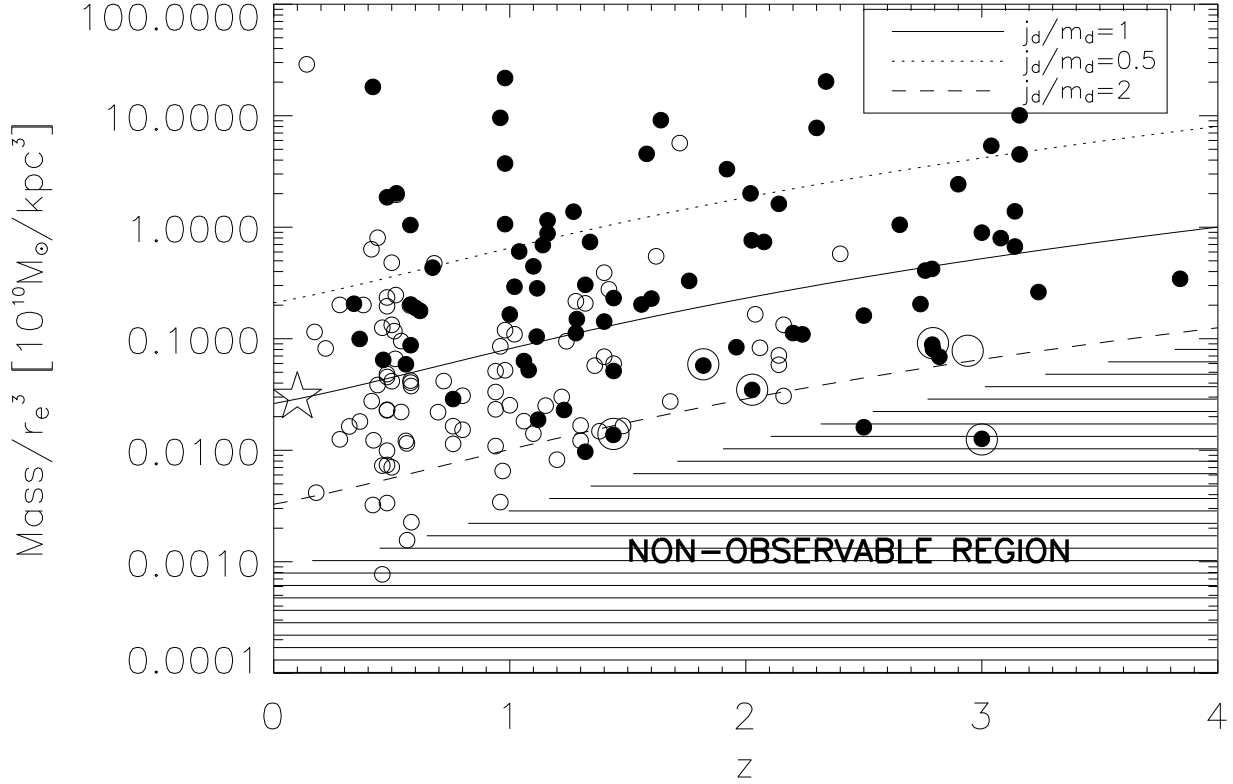


Fig. 14.— The internal density of the observed galaxies versus z . In order to make a direct comparison with the theory expectation we have used $h=0.7$. Observed galaxies are separated in two groups: solid points represent galaxies more massive than $10^{10}M_{\odot}$. These galaxies are observable over the full z range. The expected internal density M/r_e^3 of disk galaxies just formed at each redshift according to the Mo, Mau & White (1998) model is shown for three different specific angular momentum j_d/m_d values. We have used $m_d=0.05$ and $\lambda=0.05$. The internal density of the Milky Way galaxy (star) is shown for comparison. Also, we have encircled those galaxies proposed to be large disk-like galaxies at high- z following Labbé et al. (2003). Note that there is a galaxy in the Labbé et al. analysis which is not in our sample because it is outside of the field of view selected in this study.

Table 1.

Galaxy	X	Y	$K_{s,tot}$	r_e	ϵ	$L_V(10^{10} \text{ h}^{-2} L_\odot)$	$M(10^{10} \text{ h}^{-2} M_\odot)$	z	Filter
793	3538.3	3496.9	21.33	0.04	0.10	0.01	0.01	0.140	I ₈₁₄
244	2272.6	1587.5	20.71	0.40	0.67	0.06	0.09	0.173 ^a	I ₈₁₄
283	2063.5	1660.1	23.34	0.51	0.62	0.01	0.01	0.180	I ₈₁₄
314	2741.5	1815.3	21.61	0.24	0.08	0.02	0.02	0.220	I ₈₁₄
288	501.6	1633.9	23.23	0.39	0.09	0.01	0.02	0.280	I ₈₁₄
464	943.0	2017.5	20.76	0.30	0.44	0.11	0.20	0.280	I ₈₁₄
227	1393.0	1430.0	21.51	0.60	0.35	0.12	0.17	0.320	I ₈₁₄
184	626.9	1387.0	18.89	0.55	0.21	0.75	1.92	0.340 ^a	I ₈₁₄
446	2417.6	2080.2	20.05	0.56	0.36	0.39	1.11	0.364 ^a	I ₈₁₄
528	2478.4	3018.5	20.53	0.71	0.64	0.28	0.42	0.365 ^a	I ₈₁₄
53	2954.6	522.7	23.26	0.14	0.23	0.02	0.03	0.380	I ₈₁₄
663	3106.0	3832.1	21.28	0.17	0.08	0.19	0.26	0.414 ^a	I ₈₁₄
763	1258.2	3079.6	19.89	0.76	0.15	0.56	0.96	0.415 ^a	I ₈₁₄
138	3709.8	1029.9	19.83	0.14	0.40	0.48	4.08	0.420	I ₈₁₄
189	1678.4	1190.2	23.00	0.64	0.56	0.06	0.07	0.420	I ₈₁₄
256	1619.2	1632.0	21.84	0.54	0.26	0.17	0.16	0.423 ^a	I ₈₁₄
307	3037.7	1762.6	21.79	0.43	0.29	0.15	0.27	0.440	I ₈₁₄
374	1205.1	2466.3	22.80	0.13	0.22	0.03	0.16	0.440	I ₈₁₄
29	3817.2	486.8	20.58	0.34	0.24	0.64	0.48	0.460	I ₈₁₄
75	2162.5	727.1	23.14	0.94	0.05	0.08	0.06	0.460	I ₈₁₄
708	2656.4	3737.6	21.27	0.75	0.20	0.35	0.30	0.460	I ₈₁₄
292	781.1	1876.3	18.88	0.86	0.48	1.15	4.03	0.464 ^a	I ₈₁₄
87	459.7	700.5	23.26	0.29	0.30	0.05	0.05	0.480	I ₈₁₄
95	3873.2	715.5	23.33	0.11	0.30	0.05	0.03	0.480	I ₈₁₄
344	3579.9	2599.2	22.78	0.42	0.50	0.10	0.07	0.480	I ₈₁₄
415	2401.5	2278.5	21.34	0.30	0.21	0.18	0.56	0.480	I ₈₁₄
442	3236.2	2130.7	22.46	0.54	0.34	0.12	0.11	0.480	I ₈₁₄
459	3410.0	2059.1	23.14	0.19	0.17	0.08	0.03	0.480	I ₈₁₄
544	1405.0	2923.0	21.51	0.51	0.63	0.16	0.32	0.480	I ₈₁₄
673	2131.5	3486.8	22.87	0.24	0.49	0.09	0.06	0.480	I ₈₁₄
758	2271.3	3535.7	20.12	0.24	0.23	0.47	2.57	0.480	I ₈₁₄

Table 1—Continued

Galaxy	X	Y	$K_{s,tot}$	r_e	ϵ	$L_V(10^{10} \text{ h}^{-2} L_\odot)$	$M(10^{10} \text{ h}^{-2} M_\odot)$	z	Filter
766	2035.5	3411.7	22.13	0.73	0.53	0.19	0.13	0.480	I ₈₁₄
41	2006.4	560.3	21.32	0.27	0.33	0.33	0.29	0.500	I ₈₁₄
270	2703.9	1586.5	21.93	0.15	0.29	0.20	0.18	0.500	I ₈₁₄
345	3288.8	2575.0	21.74	0.71	0.00	0.23	0.28	0.500	I ₈₁₄
476	2056.1	1976.4	22.35	0.32	0.18	0.15	0.14	0.500	I ₈₁₄
91	2719.3	841.1	20.92	0.35	0.36	0.34	0.58	0.511 ^a	I ₈₁₄
339	2398.7	2627.2	21.54	0.32	0.31	0.36	0.26	0.515 ^a	I ₈₁₄
609	1716.1	3098.5	20.94	0.26	0.36	0.40	0.53	0.517 ^a	I ₈₁₄
247	4006.2	1587.3	20.35	0.17	0.16	0.67	1.26	0.520	I ₈₁₄
317	1837.8	1846.0	22.16	0.08	0.33	0.17	0.12	0.520	I ₈₁₄
482	1264.5	1950.4	22.62	0.21	0.12	0.13	0.12	0.540 ^a	I ₈₁₄
577	2577.1	2942.7	22.93	0.32	0.56	0.08	0.08	0.540	I ₈₁₄
50	3581.5	687.1	20.11	0.54	0.29	0.88	1.22	0.560 ^a	I ₈₁₄
215	3602.8	1301.6	23.12	0.42	0.43	0.07	0.11	0.560	I ₈₁₄
99	2736.9	923.1	20.93	0.72	0.62	0.42	0.56	0.564 ^a	I ₈₁₄
223	2446.8	1476.4	20.98	1.29	0.16	0.62	0.45	0.565 ^a	I ₈₁₄
234	2859.3	1472.7	20.28	0.33	0.26	0.51	0.96	0.577 ^a	I ₈₁₄
549	2982.7	2839.3	19.51	0.30	0.15	1.54	4.11	0.579 ^a	I ₈₁₄
153	3459.5	1028.6	22.46	0.31	0.67	0.15	0.16	0.580	I ₈₁₄
193	3572.2	1508.4	18.11	0.73	0.34	4.64	11.0	0.580 ^a	I ₈₁₄
409	1750.0	2270.8	19.46	0.55	0.09	1.72	2.07	0.580 ^a	I ₈₁₄
770	3363.7	3511.1	22.00	0.34	0.61	0.20	0.23	0.580 ^a	I ₈₁₄
410	1808.7	2284.3	22.01	0.38	0.12	0.24	0.30	0.582 ^a	I ₈₁₄
427	2718.8	2204.3	20.86	1.30	0.14	0.63	0.69	0.583 ^a	I ₈₁₄
645	1839.4	4121.8	20.55	0.38	0.19	1.00	1.50	0.600	I ₈₁₄
30	1189.3	478.1	21.45	0.37	0.25	0.26	1.40	0.620	I ₈₁₄
684	2099.1	3636.9	20.02	0.36	0.29	1.27	3.52	0.673 ^a	I ₈₁₄
297	1827.8	1697.9	22.06	0.21	0.30	0.17	0.75	0.680	I ₈₁₄
198	832.7	1263.0	21.61	0.43	0.32	0.57	0.30	0.696 ^a	I ₈₁₄
65	995.6	654.3	23.05	0.24	0.66	0.17	0.10	0.720	I ₈₁₄
394	3953.7	2367.7	20.39	0.35	0.37	2.51	0.09	0.760	I ₈₁₄

Table 1—Continued

Galaxy	X	Y	$K_{s,tot}$	r_e	ϵ	$L_V(10^{10} \text{ h}^{-2} L_\odot)$	$M(10^{10} \text{ h}^{-2} M_\odot)$	z	Filter
610	1674.7	3067.4	19.95	0.84	0.28	1.66	3.46	0.760 ^a	I ₈₁₄
768	2591.1	3492.9	23.36	0.30	0.67	0.13	0.08	0.760	I ₈₁₄
774	2782.2	3544.1	22.43	0.39	0.43	0.33	0.19	0.800	I ₈₁₄
777	1520.1	3463.8	22.06	0.34	0.24	0.60	0.25	0.800	I ₈₁₄
306	1129.4	1783.3	22.85	0.43	0.70	0.42	0.20	0.940	J _s
337	3929.8	2643.0	21.82	0.39	0.08	1.08	0.74	0.940	J _s
638	2661.3	4089.3	23.02	0.28	0.42	0.24	0.12	0.940	J _s
795	1214.5	3434.2	23.37	0.24	0.32	0.21	0.10	0.940	J _s
64	2166.0	660.9	22.25	0.28	0.10	0.54	0.48	0.960	J _s
268	1288.8	1574.3	22.10	0.09	0.15	0.37	1.83	0.960	J _s
367	3558.3	2506.5	23.23	0.60	0.16	0.27	0.18	0.960	J _s
429	581.0	2211.8	21.79	0.75	0.73	0.82	0.68	0.970 ^a	J _s
97	3335.8	784.7	20.85	0.10	0.02	2.08	5.25	0.980	J _s
301	1390.5	1700.6	23.15	0.22	0.26	0.24	0.14	0.980	J _s
326	1654.8	2678.6	22.16	0.19	0.11	0.40	1.77	0.980	J _s
420	2836.4	2263.4	21.69	0.15	0.14	0.61	3.02	0.980	J _s
691	3374.1	3822.9	22.63	0.24	0.23	0.39	0.39	0.980	J _s
608	3122.9	4270.2	22.18	0.41	0.22	0.61	0.42	1.000	J _s
665	2535.8	3888.0	21.64	0.44	0.42	0.70	3.58	1.000	J _s
224	2397.5	1376.9	21.82	0.24	0.24	0.56	1.08	1.020	J _s
753	2850.8	3602.0	22.89	0.22	0.17	0.41	0.29	1.020	J _s
10008	342.7	1274.3	22.32	0.19	0.38	0.32	1.05	1.040	J _s
152	1123.2	994.5	23.00	0.40	0.35	0.43	0.31	1.060	J _s
241	2508.8	1585.0	21.71	0.46	0.36	0.74	1.56	1.060	J _s
79	3159.3	746.3	21.48	0.46	0.44	1.24	1.38	1.080	J _s
18	1361.7	404.4	21.20	0.30	0.11	1.09	3.28	1.100	J _s
249	2222.5	1495.3	22.59	0.55	0.28	0.29	0.63	1.100	J _s
565	2534.7	2935.8	20.75	0.47	0.32	2.31	2.92	1.114 ^a	J _s
686	2474.7	3767.0	21.06	0.33	0.19	1.57	2.82	1.116 ^a	J _s
493	271.4	1901.0	20.97	0.74	0.40	1.60	2.02	1.120	J _s
45	3166.5	573.0	20.89	0.28	0.01	2.04	4.08	1.140	J _s

Table 1—Continued

Galaxy	X	Y	$K_{s,tot}$	r_e	ϵ	$L_V(10^{10} \text{ h}^{-2} L_\odot)$	$M(10^{10} \text{ h}^{-2} M_\odot)$	z	Filter
206	3136.3	1280.3	22.71	0.36	0.25	0.67	0.33	1.152 ^a	J _s
276	2216.7	1691.8	20.89	0.27	0.20	2.00	6.13	1.160	J _s
644	3261.3	3967.9	22.67	0.21	0.00	0.40	2.24	1.160	J _s
669	2412.0	3968.5	23.27	0.47	0.06	0.46	0.23	1.200	J _s
404	3693.2	2330.4	22.75	0.41	0.26	0.65	0.59	1.220	J _s
27	956.2	585.7	20.22	1.07	0.08	4.25	8.05	1.230 ^a	J _s
251	765.4	1492.1	22.79	0.30	0.77	0.54	0.70	1.240	J _s
254	2579.9	1701.3	20.31	0.27	0.13	4.96	7.81	1.270 ^a	J _s
101	1314.3	781.9	22.23	0.35	0.35	1.21	1.43	1.280	J _s
149	2849.3	951.4	23.18	0.23	0.16	0.29	0.74	1.280	J _s
470	2606.8	1988.5	20.39	0.52	0.03	3.93	6.13	1.284 ^a	J _s
502	1804.0	1838.1	23.20	0.46	0.66	0.33	0.47	1.300	J _s
771	3494.8	3469.8	22.85	0.58	0.43	0.45	0.69	1.300	J _s
145	1432.7	983.2	22.34	0.71	0.32	0.74	1.00	1.320	J _s
395	2926.7	2377.6	22.65	0.24	0.13	0.90	0.85	1.320	J _s
637	2746.6	4100.2	21.94	0.27	0.48	1.68	1.81	1.320	J _s
199	1544.7	1257.0	21.68	0.31	0.18	1.29	6.27	1.340	J _s
791	2767.9	3454.1	22.97	0.33	0.47	0.58	0.58	1.360	J _s
437	3508.0	2173.2	23.15	0.51	0.52	0.58	0.58	1.380	J _s
201	3955.7	1215.0	22.96	0.32	0.18	0.99	0.64	1.400	J _s
408	1297.5	2325.2	23.08	0.17	0.20	0.75	0.56	1.400	J _s
785	3438.1	3196.3	21.57	0.43	0.23	2.16	3.33	1.400	J _s
751	2004.1	3687.6	23.13	0.21	0.13	0.69	0.80	1.420	J _s
302	770.9	1799.8	21.55	0.94	0.10	2.94	3.36	1.439 ^a	J _s
61	3804.3	592.7	23.02	0.34	0.25	0.58	0.68	1.440	J _s
783	2674.2	3530.1	22.50	0.26	0.19	0.86	1.21	1.440	J _s
10001	2954.3	782.1	21.53	0.59	0.24	2.50	3.16	1.440	J _s
781	1304.1	3494.1	22.72	0.53	0.53	1.08	0.75	1.480	J _s
620	1876.8	3623.2	22.16	0.29	0.12	2.27	1.48	1.558 ^a	H
628	3265.9	4251.8	22.37	0.13	0.10	1.15	3.18	1.580	H
675	1836.0	3395.8	22.22	0.32	0.18	1.61	2.17	1.600	H

Table 1—Continued

Galaxy	X	Y	$K_{s,tot}$	r_e	ϵ	$L_V(10^{10} \text{ h}^{-2} L_\odot)$	$M(10^{10} \text{ h}^{-2} M_\odot)$	z	Filter
724	2272.9	3717.9	23.34	0.17	0.37	0.56	0.75	1.620	H
583	3745.2	3064.7	22.90	0.12	0.19	0.88	4.36	1.640	H
349	1064.0	2559.4	23.17	0.40	0.28	1.06	0.51	1.680	H
233	1148.6	1369.4	23.38	0.07	0.44	1.03	0.70	1.720	H
754	2616.4	3525.4	23.16	0.26	0.36	0.73	1.80	1.760	H
267	966.0	1628.1	21.83	0.58	0.26	3.42	3.39	1.820	H
810	3062.8	3348.3	22.80	0.14	0.12	1.17	2.69	1.920	H
600	1843.5	3658.4	22.32	0.52	0.33	2.94	3.49	1.960	H
500	2364.1	1852.0	23.24	0.15	0.54	0.89	1.91	2.020	H
290	696.4	1684.2	21.95	0.27	0.11	4.66	2.54	2.025 ^a	H
257	3011.6	1696.2	22.10	0.61	0.43	3.75	2.27	2.027 ^a	H
21	2416.4	406.0	23.49	0.20	0.54	1.15	0.39	2.040	H
96	375.0	716.1	23.35	0.30	0.57	1.40	0.56	2.060	H
776	3562.4	3421.4	22.44	0.21	0.16	2.82	1.96	2.077 ^a	H
173	572.9	1026.0	23.23	0.35	0.23	1.41	0.86	2.140	H
496	373.2	1877.0	22.40	0.21	0.13	2.40	4.49	2.140	H
729	3327.2	3768.1	22.73	0.38	0.31	2.51	0.91	2.140	H
143	779.7	969.2	23.37	0.48	0.34	1.41	0.94	2.160	H
242	1139.5	1425.8	23.43	0.25	0.17	1.25	0.55	2.160	H
219	3888.0	1291.8	23.35	0.35	0.62	1.27	1.35	2.200	H
375	1210.7	2405.4	22.79	0.47	0.21	2.01	3.14	2.240	H
767	3297.6	3622.1	22.54	0.17	0.41	3.06	10.1	2.300	H
161	2577.8	985.6	23.42	0.10	0.40	1.30	5.55	2.340	H
591	3936.8	3251.8	19.56	0.18	0.16	1.49	0.94	2.400	H
176	722.5	1089.1	22.92	0.46	0.24	2.79	4.11	2.500	H
363	537.5	2521.3	22.41	0.78	0.24	4.72	2.00	2.500	H
10006	3127.6	985.8	23.32	0.18	0.23	2.43	1.41	2.652 ^a	K_s
656	2535.7	4060.5	22.69	0.68	0.21	4.21	15.2	2.740	K_s
452	567.0	2083.6	22.84	0.31	0.57	4.13	3.06	2.760	K_s
806	3266.3	3256.9	22.67	0.26	0.30	4.91	1.76	2.789 ^a	K_s
807	3305.0	3263.3	22.70	0.45	0.14	4.86	1.86	2.790 ^a	K_s

Table 1—Continued

Galaxy	X	Y	$K_{s,tot}$	r_e	ϵ	$L_V(10^{10} \text{ h}^{-2} L_\odot)$	$M(10^{10} \text{ h}^{-2} M_\odot)$	z	Filter
657	3370.9	4068.2	22.53	0.57	0.26	5.94	3.51	2.793 ^a	K_s
294	382.4	1662.5	23.34	0.49	0.10	2.81	1.95	2.820	K_s
453	3945.9	2085.7	23.27	0.24	0.12	2.99	8.15	2.900	K_s
534	3452.7	2959.4	22.78	0.28	0.31	5.35	4.52	3.000	K_s
494	2562.2	1910.4	22.99	0.93	0.31	4.47	2.28	3.000	K_s
465	360.7	2029.8	23.37	0.14	0.71	3.13	3.27	3.040	K_s
397	2460.0	2379.0	23.41	0.32	0.46	3.17	5.91	3.080	K_s
448	2508.9	2111.6	23.46	0.16	0.41	2.78	1.25	3.140	K_s
622	3299.0	4292.6	23.07	0.24	0.37	3.90	1.95	3.140	K_s
98	4055.0	718.8	23.09	0.16	0.16	4.65	9.66	3.160	K_s
624	3738.7	4243.9	23.19	0.21	0.16	4.22	9.01	3.160 ^a	K_s
813	2779.1	3315.0	23.31	0.29	0.43	3.14	1.39	3.240	K_s
80	2926.6	703.1	22.71	0.40	0.11	8.88	3.71	3.840	K_s

Note. — Col. (1): Catalog identification numbers (see Labbé et al. 2003). Col. (2) and (3): X and Y pixel coordinate positions in the HDF–S mosaic. Col (4): K_s –band total magnitudes. Col. (5): Circularized restframe half–light radii (arcsec). The typical uncertainty on the size determination is 35%. Col (6): intrinsic (i.e. the recovered non–seeing affected) ellipticity. Col (7): Restframe V–band luminosity. The typical uncertainty on the luminosity determination is 30%. Col (8): Stellar mass. Col (9): redshift (the index *a* mean spectroscopic *z*). Col (10): Filter used to measure the size of the galaxies

Table 2.

$L_V(10^{10} \text{ h}^{-2} L_\odot)$ (1)	$\bar{r}_e(L, 0)$ (2)	$\sigma(L, 0)$ (3)	z' (4)	$\bar{r}_e(L, z = 2.5)/\bar{r}_e(L, 0)$ (5)
3–10	6.45	0.36	3.91	0.25(± 0.10)
1–3	3.68	0.33	2.58	0.35(± 0.10)
0.3–1	2.07	0.40	1.55	–
$M(10^{10} \text{ h}^{-2} M_\odot)$	$\bar{r}_e(M, 0)$	$\sigma(M, 0)$	z'	$\bar{r}_e(M, z = 2.5)/\bar{r}_e(M, 0)$
3–10	2.46	0.44	3.17	0.60(± 0.15)
1–3	1.94	0.49	2.52	0.80(± 0.20)
0.3–1	1.70	0.52	1.70	–

Note. — Properties of the bin selection for analyzing the evolution of sizes in the FIRES data. Col. (1): the luminosity (mass) range of the bin. Col. (2): SDSS mean size (in $\text{h}^{-1} \text{ kpc}$) at $z \sim 0$ of galaxies with a luminosity equal to the mean luminosity of the FIRES galaxies in the luminosity (mass) range of Col. (1). Col. (3): Same than in Col. (2) but with the SDSS dispersion. Col. (4): Largest observable redshift (for galaxies with $K_S < 23.5$) for the mean luminosity (mass) of the analyzed bin. Col. (5): Implied size evolution at $z=2.5$ according to our analysis (see text for details).